Journal of Nuclear Medicine, published on January 31, 2020 as doi:10.2967/jnumed.119.233072

Title: Demarcation of Sepsis-Induced Peripheral and Central Acidosis with pH-Low Insertion Cyclic (pHLIC) Peptide

Running Title: Demarcating Acidosis with pH-Targeted PET

Kelly E. Henry,[1] Aisling M. Chaney,[2] Veronica L. Nagle,[1,3,4] Haley C. Cropper,[2] Saghar Mozaffari,[5] Gregory Slaybaugh,[6] Keykavous Parang,[5] Oleg A. Andreev,[6] Yana K. Reshetnyak,[6] Michelle L. James,[2,7*] Jason S. Lewis[1,3,4,8*]

[1]Department of Radiology, Memorial Sloan Kettering Cancer Center, New York, NY

[2]Department of Radiology, Stanford University, Stanford, CA

[3]Molecular Pharmacology Program, Memorial Sloan Kettering Cancer Center, New York, NY

[4]Departments of Pharmacology and Radiology, Weill Cornell Medical College, New York, NY

[5]Center for Targeted Drug Delivery, Department of Biomedical and Pharmaceutical Sciences, Chapman University School of Pharmacy, Irvine, CA

[6]Department of Physics, University of Rhode Island, Kingston, RI

[7]Department of Neurology & Neurological Science, Stanford University, Stanford, CA

[8]Radiochemistry and Molecular Imaging Probes Core, Memorial Sloan Kettering Cancer Center, New York, NY

M.L.J. -- mljames@stanford.edu, P: 650-497-0153; F: 650-724-4948 *Co-corresponding author

J.S.L. -- lewisj2@mskcc.org, P: 646-888-3038, F: 646-888-3059, *Co-corresponding author

K.E.H. -- henryk1@mskcc.org, P: 646-888-3271, F: 646-888-3059, Postdoctoral Research Fellow

Financial support: See acknowledgements section.

Word Count: 4725

ABSTRACT:

Acidosis is a key driver for many diseases, including cancer, sepsis, and stroke. The spatiotemporal dynamics of dysregulated pH across disease remains elusive and current diagnostic strategies do not provide localization of pH alterations. We sought to explore if PET imaging using hydrophobic cyclic peptides that partition into the cellular membrane at low extracellular pH (denoted as “pHLIC”) can permit accurate in vivo visualization of acidosis.

Methods: Acid-sensitive cyclic peptide c[E_4W_5C] pHLIC was conjugated to bifunctional maleimide-NO2A and radiolabeled with copper-64 ($t_{½}$ = 12.7 h). C57BL/6J mice were administered LPS (15 mg/kg) or saline (vehicle) and serially imaged with [^{64}Cu]Cu-c[E_4W_5C] over 24 h. Ex vivo autoradiography was performed on resected brain slices and subsequently stained with cresyl violet to enable high-resolution spatial analysis of tracer accumulation. A non- pH-sensitive cell-penetrating control peptide (c[R_4W_5C]) was used to confirm specificity of [^{64}Cu]Cu-c[E_4W_5C]. CD11b (macrophage/microglia) and TMEM119 (microglia) immunostaining was performed to correlate extent of neuroinflammation with [^{64}Cu]Cu-c[E_4W_5C] PET signal.

Results: [^{64}Cu]Cu-c[E_4W_5C] radiochemical yield and purity was >95% and >99% respectively, with molar activity >0.925 MBq/nmol. Significantly increased [^{64}Cu]Cu-c[E_4W_5C] uptake was observed in LPS-treated mice (vs. vehicle) within peripheral tissues including blood, lungs, liver, and small intestines (P < 0.001-0.05). Additionally, there was significantly increased [^{64}Cu]Cu-c[E_4W_5C] uptake in the brains of LPS-treated animals. Autoradiography confirmed increased uptake in the cerebellum, cortex, hippocampus, striatum, and hypothalamus of LPS-treated mice (vs. vehicle). Immunohistochemical

(IHC) analysis revealed microglial/macrophage infiltrate, suggesting activation in brain regions containing increased tracer uptake. [^{64}Cu]Cu-c[R_4W_5C] demonstrated significantly reduced uptake in the brain and periphery of LPS mice compared to the acid-mediated [^{64}Cu]Cu-c[E_4W_5C] tracer.

Conclusion: Here, we demonstrate that a pH-sensitive PET tracer specifically detects acidosis in regions associated with sepsis-driven pro-inflammatory responses. This study suggests that [^{64}Cu]Cu-pHLIC is a valuable tool to noninvasively assess acidosis associated with both central and peripheral innate immune activation.

KEY WORDS: Acidosis, Neuroinflammation, Sepsis, pHLIC, Copper-64

INTRODUCTION

Maintenance of physiological pH is crucial for cellular homeostasis and is closely linked to innate immunological function (*1, 2)*. When an acid-base imbalance occurs and blood/tissue pH becomes acidic – a condition known as acidosis – cellular and immune dysfunction can occur, resulting in a potentially life-threatening pathogenic state (*3, 4)*. Acidosis is one of the most common diagnoses seen in patients suffering from critical illness including cardiovascular disease, stroke, and sepsis, ultimately resulting in an overabundance of protons in the extracellular medium (*5, 6*). These protons can interact with receptors on innate immune cells (e.g. monocytes, macrophages and natural killer cells) to drive inflammatory responses (*5, 6)*. Both immune activation and suppression have been reported as a result of acidosis with low pH differentially affecting immune responses depending on cell type and pathways being investigated (*1, 2, 6*). Pathologic acidosis and inflammation in peripheral tissues can trigger microglia activation in the central nervous system (CNS), implicating an important role for the crosstalk between acid-sensing ion channels (ASICs) and the immune system in neuroinflammatory diseases (*1, 7*).

Efficient localization of acidosis has potential to greatly impact disease management and patient outcomes (*3, 8*). Currently, acidosis is identified via urine sampling (ketoacidosis) and/or arterial blood collection (*4, 9*). Although these techniques provide confirmation on physiological state, neither afford region-specific information regarding the pathologically affected tissues, hence accurate diagnosis and localization can be challenging (*4, 10*). Metabolic acidosis is a common clinical pathology that manifests in different ways, affecting a breadth of tissues (*11, 12*), and can acutely affect

the CNS (*13*). Since CNS biopsies are extremely invasive, there is an unmet need to noninvasively quantify acidosis in the brain and whole-body. Therefore, we sought to develop a probe to specifically detect acidosis with high sensitivity and identify whole-body/brain acid-base alterations, allowing for more informed clinical decisions and disease management.

Previously, we developed a novel class of molecules known as pH (Low) Insertion Peptides (pHLIPs®) that target acidity and utilize a mechanism that does not rely on the selective efficacy of other biomarker technologies (*e.g.* the need for receptor upregulation at a specific site of disease to delineate from non-target tissues) (*14*). The pHLIP family of peptides have thus far shown utility in tumor imaging and delivery of therapeutic agents (*15-17*). The mechanism of pHLIP entails protonation of negatively-charged residues on a disordered linear peptide sequence in the acidic extracellular microenvironment, resulting in enhancement of peptide hydrophobicity and insertion into phospholipid bilayer of the cell membrane forming a stable transmembrane alpha helix (*14*). This pH-sensitive concept was leveraged to develop a novel class of cyclic peptides (pH (Low) Insertion Cycles, or pHLIC) for enhanced enzymatic stability versus linear peptides (*18*). These cyclic versions consist of negatively charged glutamate residues located at one side of the cycle and hydrophobic tryptophan residues on the other (*19*). The glutamate residues are protonated at low extracellular pH to allow for better diffusion of pHLIC into the membrane. When equilibrium is established, glutamate residues are de-protonated in cytoplasm preventing pHLIC from exiting the membrane and anchoring cycles into the lipid bilayer.

Since pHLICs possess promising characteristics for blood-brain barrier (BBB) penetration (i.e., inherently hydrophobic and relatively small size), we chose to explore a positron emission tomography (PET) labeled version of a novel pHLIC peptide. We selected the lipopolysaccharide (LPS)-induced mouse model of sepsis, as it is known to exhibit alterations in pH, extensive systemic inflammation, and brain microglial activation (*5, 6, 20, 21*).

The aims of this study were to investigate the utility of our novel pH-sensitive probe, [^{64}Cu]Cu-c[E_4W_5C] pHLIC, for tracking acidosis in LPS versus saline-treated mice over the course of 24 h. The central hypothesis was that pH-targeted cyclic peptide probe ([^{64}Cu]Cu-c[E_4W_5C]) will successfully demarcate acidosis through PET and correspond with ex vivo brain uptake and macrophage/microglial activation. In order to confirm our probe's specificity for the acidic microenvironment, we included a [^{64}Cu]Cu-c[R_4W_5C] probe as a negative control. Arginine residues (instead of glutamate in the pH-sensitive peptide) will facilitate a cell-penetrating (*22*), but not via a pH-sensitive mechanism of insertion.

We emphasize that it is not a facile process to take a biopsy of brain tissue. The innovation of this work lies in the ability to noninvasively collect a breadth of information regarding sepsis-induced acidosis in the whole-body and brain longitudinally using our newly developed PET radiotracer to shed light on the complexities of acidosis.

MATERIALS AND METHODS

Materials. All materials were purchased from Sigma-Aldrich (St. Louis, MO), unless otherwise described.

Synthesis of pHLIC-NO2A Construct. Peptides were designed and synthesized in the Andreev, Reshetnyak, and Parang labs using solid-phase peptide synthesis techniques (see Supplemental Fig. 1-4). Cyclic peptides were conjugated to NO2A-maleimide using previously reported methods and is further detailed in the supporting materials (*16*). Both pHLIC constructs were chosen for in vivo studies due to their favorable LogP value (Supplemental Table 1) for BBB penetration (*23*). Cyclic peptide c[E_4W_5C] proceeded further due to pilot experiments showing more favorable BBB penetration, CNS biodistribution, and peripheral detection of acidosis in mice. Doses for animal experiments were diluted in PBS to a maximum concentration of 5% ethanol.

Radiolabeling of pHLIC-NO2A. [^{64}Cu]$CuCl_2$ was obtained from University of Wisconsin Madison (Stanford) and the University of Washington St. Louis (MSK). Each experiment included [^{64}Cu]$CuCl_2$ controls to ensure reproducibility between experiments and institutions. pHLIC-NO2A (20 μL, 16 nmol) was diluted in 0.1 M NH_4Ac (pH 5.5) and was incubated with [^{64}Cu]$CuCl_2$ (14-15 MBq) at 80 °C for 15 min. [^{64}Cu]Cu-c[E_4W_5C] was purified using a C_{18} Sep Pak with 100% ethanol elution. Radiochemical purity was assessed using instant thin later chromatography using a 50 mM EDTA (pH 5) eluent. Partition coefficient experiments proceeded in a PBS:octanol mixture using previously reported techniques (*24*). Cold labeling of pHLIC-NO2A along with a description of the biophysical measurements of ^{nat}Cu-c[E_4W_5C] and ^{nat}Cu-c[R_4W_5C] can be found in the Supplementary Materials.

Animal models. All animal experiments were performed in accordance with the Stanford Administrative Panel on Laboratory Animal Care (APLAC), which is accredited by the Association for the Assessment and Accreditation of Laboratory Animal Care (AAALAC

International) or the Institutional Animal Care and Use Committee at Memorial Sloan Kettering Cancer Center. LPS (*Escherichia coli*) at a concentration of 3 mg/kg in sterile saline was injected intraperitoneally (i.p.) in female C57BL/6J mice (6-8 weeks old, Jackson Laboratories) 3 h prior to [^{64}Cu]Cu-c[E_4W_5C] administration (15 mg/kg). Saline was used as a vehicle control.

PET/CT Imaging. Radiotracer (16-20 nmol, 14-15 MBq in sterile PBS, 130-150 μL) was injected intravenously and 10 min static PET/CT images were acquired at 1, 5, 9, and 20 h (4, 8, 12, and 24 h post-LPS inoculation) using a dual microPET/CT scanner (Inveon, Siemens). PET timepoints with [^{64}Cu]Cu-pHLIC were adapted from a time course previously established by Demoin et al. (*16*). Brain PET quantitation was completed using VivoQuant software (version 3.0, InviCRO) as described previously (*25*). Rodent anesthesia for both institutions was isoflurane, supplemented with either pure oxygen (Stanford) or medical air (MSK). Scan time at MSK varied to achieve the same number of coincidence events to acquire high resolution PET images at every time point. Please note the Disclaimer of Variability Between Institutions in the Supplementary Information to understand how this may affect baseline radiotracer uptake.

Biodistribution studies. Blood was collected via cardiac puncture prior to PBS perfusion. Brain and other tissues were harvested and weighed wet. Radioactivity within each organ was counted using a Hidex Automatic γ-counter. Tracer uptake expressed as percentage injected dose per gram (% ID/g) was calculated as the radioactivity in each tissue divided by the organ mass and the decay-corrected injected dose at the time of counting, as determined by a calibration curve established via serial dilutions of the ^{64}Cu-labelled peptide.

Autoradiography. Ex vivo autoradiography was performed as described previously (*26*) using 40 μm-thick left-hemisphere coronal brain sections collected at 12 and 24 h post-injection of LPS. Anatomy was confirmed by Nissl staining (cresyl violet acetate), using standard techniques. After exposing tissues to digital autoradiography films for 10 half-lives, each film was scanned using a Typhoon phosphorimager. ImageJ software version 2.0.0 was used to visualize images.

Immunohistochemistry. For semiquantitative evaluation of activated microglia and inflammation, staining of CD11b and TMEM119 was performed on 5 μm coronal brain sections, respectively, using previously described methods (*26, 27*).

Statistical Considerations. GraphPad Prism (version 7; GraphPad Software) was used for statistical analyses of the data. Biodistribution data were analyzed by unpaired, two-tailed Student's *t*-tests and differences at the 95% confidence level. All other data were analyzed via 1-way or 2-way ANOVAs with multiple comparisons. P values of 0.05 or less were considered significant.

RESULTS

Synthesis, Radiolabeling, and Biophysics of pHLIC. Peptide-chelator conjugates c[E_4W_5C]-NO2A and c[R_4W_5C]-NO2A were produced in 55-60% yield with >99% purity. Mass spectrometry analyzed appropriate peaks before each subsequent step. MALDI-ToF results: c[E_4W_5C]-NO2A $[M+H]^+$ = m/z: 1977.21 *m/z*; c[R_4W_5C]-NO2A $[M+H]^+$ = m/z: 2085.11 *m/z*. LCMS results: [^{nat}Cu]Cu-c[E_4W_5C] $[M+5H]^+$ = m/z: 428.2 *m/z*; [^{nat}Cu]Cu-c[R_4W_5C] $[M+5H]^+$ = 446.7 m/z: *m/z*. Radiochemical yield and molar activity for all pHLIC conjugates were >95% and >0.925 MBq/nmol respectively. Radiochemical purity was

>99% for all peptide conjugates (Supplemental Fig. 4), and [^{64}Cu]Cu-c[E_4W_5C] was >90% stable in serum out to 48 h (Supplemental Fig. 5). Measured Log P values of [^{64}Cu]Cu-c[E_4W_5C] were found to be 2.5 $\pm$ 0.6 at pH 6 and 2.0 $\pm$ 0.2 at pH 7.4 (*n* = 5 replicates per run; 3 independent measurements) (Supplemental Table 1). Biophysical studies of and showed a pH dependence of ^{nat}Cu-c[E_4W_5C], but not of ^{nat}Cu-c[R_4W_5C], indicating pH sensitivity of our pHLIC radiotracer (Supplemental Fig. 6).

In Vivo Study Design. The onset of acidosis has been reported to manifest peripherally as early as 4 h post-LPS injection, hence we chose this as our first timepoint to study the pharmacokinetics of our radiotracer (*21*). Microglial activation occurs within 24 h post-LPS administration in mice (*7, 28*). In order to study alterations in acidosis-induced inflammation over time, [^{64}Cu]Cu-c[E_4W_5C] was injected 3 h post-LPS induction and static PET images were acquired at 1, 5, 9, and 21 h post-radiotracer injection (corresponding to 4, 8, 12, and 24 h post-LPS induction). Fig. 1 illustrates this workflow along with the mechanism of pHLIC peptides' interaction with membrane during acidotic conditions.

PET and Ex Vivo Biodistribution. Serial PET images acquired over 24 h show a clear difference in peripheral [^{64}Cu]Cu-c[E_4W_5C] uptake in vehicle vs. LPS-treated mice (Fig. 2) in tissues affected by acidosis. Less uptake and brain specificity were observed with [^{64}Cu]Cu-[E_5K]W_5C vs. [^{64}Cu]Cu-c[E_4W_5C] PET (Supplemental Fig. 7 and 8, Supplemental Tables 2 and 3), hence the rationale for moving forward with [^{64}Cu]Cu-c[E_4W_5C] for all subsequent studies. CT-guided PET quantitation demonstrated significant increases in [^{64}Cu]Cu-c[E_4W_5C] uptake in the kidneys, liver, lungs, and small intestine of LPS mice over 24 h (Fig. 2). Each of these tissues demonstrated significantly higher uptake of radiotracer in LPS mice at all timepoints except in kidneys at 4 h post-

LPS injection. Ex vivo biodistribution (for 12 and 24 h, Supplemental Table 3) supports the in vivo findings (*n* = 4/group). PET quantitation of selected regions is represented in Supplemental Table 4 (*n* = 4/group). Zoomed in rescaled images show uptake of [^{64}Cu]Cu-c[E_4W_5C] in the brain are represented in Fig. 3 for 12 and 24 h timepoints and show significant uptake in LPS vs. vehicle-treated animals. Full PET quantification, additional time points, and coronal brain views can be found in Supplemental Figs. 9-12. Supplemental Fig. 13 represents the brain atlas legend for the inviCRO PET quantification.

A statistically significant ($P < 0.001$-0.05) increase in [^{64}Cu]Cu-c[E_4W_5C] uptake was observed in the brain of LPS-treated mice (vs. vehicle) in several regions, many of which have been reported to exhibit inflammation (cerebellum, cortex, hippocampus, hypothalamus, striatum, and midbrain) in this model (Fig. 3) (*7, 29-32*). Full PET quantitation (of all brain regions) can be found in Supplemental Table 5 for all time points. A repeat cohort of [^{64}Cu]Cu-c[E_4W_5C] was done in tandem with negative control tracer [^{64}Cu]Cu-c[R_4W_5C] to highlight specificity of our pHLIC radtiotracer for acidosis (Fig. 4). Full ex vivo quantification for these studies (brain and periphery) studies can be found in Supplemental Figs. 14-18 and Supplemental Tables 6-8.

Autoradiography. Qualitative autoradiography of brain slices confirmed increased uptake of the radiotracer in the cerebellum, cortex, hippocampus, and hypothalamus of LPS-treated mice (vs. vehicle) (Fig. 5). Many of these regions have shown to be affected by neuroinflammation in this model (*7, 29*). Marked signal was also observed in the choroid plexus and ventricles of both vehicle and LPS-treated mice. In an additional

cohort we demonstrated significant uptake of [^{64}Cu]Cu-c[E_4W_5C] vs. negative control peptide [^{64}Cu]Cu-c[R_4W_5C] in a number of these same regions (Fig. 6).

Immunohistochemistry. Brains immunostained for CD11b and TMEM119 24 h post-LPS treatment showed increased macrophage/microglia cells. Significantly increased $CD11b^+$ cell numbers (coupled with a more ameboid-like morphology) in the hippocampus was observed in LPS-treated mice (vs. vehicle) (Fig. 7). A qualitative increase in macrophage/microglia was also observed in the hypothalamus and cortex. A subtle increase in TMEM119 represents increased innate immune infiltration that is specific to microglia (*33*) in the cortex and striatum (Supplemental Fig. 19). This data aligns with previous reports demonstrating increased neuroinflammation in the LPS model correlating to innate immune activation (*5, 34, 35*) and mirrors the increased uptake of [^{64}Cu]Cu-c[E_4W_5C] observed via PET and autoradiography in LPS-treated mice.

DISCUSSION

We report the first investigation of a pH-sensitive PET tracer for tracking acidosis in a murine model of sepsis. We have shown the potential of this tool to shed light on the connection between acidosis and innate immune activation over the course of 24 h during the onset of sepsis. Such a radiotracer could enable disease tracking not only in sepsis but in other disorders that exhibit acidosis, including diabetes and stroke. Our study identified acid-base imbalances in the periphery and the brain by targeting the acidic microenvironment, a specific danger signal in sepsis, and explored the connection between acidosis and neuroinflammation.

Acidosis is currently poorly understood with regard to whole-body progression, specific regional involvement, and interventions (*4, 12)*. One approach being explored to assess the spatiotemporal dynamics of acidosis is Chemical Exchange Saturation Transfer (CEST) magnetic resonance imaging (MRI), and is well-described by Pagel and coworkers (*36*). CEST-MRI exploits a specific MR frequency to generate an image while combining the specificity of magnetic resonance spectroscopy with the spatial resolution of MRI (*37*). Recently, CEST-MRI was combined with [^{18}F]FDG PET to explore the relationship between acidosis and hyperglycolysis within the tumor microenvironment (*38*) and a correlation between low extracellular pH and glucose uptake was identified. We have observed a similar correlation with various pHLIP variants (unpublished data). Additionally, several groups have paved the way for hyperpolarized MR imaging of metabolic acidosis, including for neuroinflammatory disorders (*39, 40*). However, hyperpolarized MR presents technical challenges for clinical translation due to its rapid signal decay. Our pH-sensitive PET agent utilizes a single dose to assess acidosis and obtain dynamic information of a system in constant flux with ultra-high sensitivity.

The most attractive application of pHLIP/pHLIC imaging platforms is the ability to target highly dynamic changes in the acidic microenvironment without needing to wait for slower changes in expression of a specific receptor. The design of our radiotracer includes a single point of conjugation, which does not affect the properties of its pH-targeting capabilities (*19*) or ability to cross the BBB, the former further evidenced by our biophysical measurements (Supplemental Fig. 6). Once acidosis has gone beyond peripheral damage to affect the CNS, it poses a much more critical clinical situation (*13*), hence early and spatiotemporal detection is crucial. Among the tested pHLIPs and

pHLICs, c[E_4W_5C] showed the best BBB penetration and highest sensitivity for detecting disease-associated pH alterations, and was therefore selected for detailed investigation. In this study, we exploited the sensitive, quantitative, and longitudinal characteristics of PET imaging to understand both spatial and temporal dynamics of acidosis.

The molecular mechanisms of how pH imbalance leads to cell damage are both diverse and complicated. Adversarial pH changes outside physiological norm can affect a number of biochemical systems, including cell development and degradation, energy metabolism, and neuronal function (e.g. metabolism of transmitter constituents) (*12*). Studies have reported the consequences of metabolic acidosis and how it affects tissues such as the liver, kidneys, and intestines (*12, 41*). ASICs are activated in the presence of inflammation, further perpetuating adverse immune responses, which can lead to significant neuroinflammation over the course of 24 h (7, 35). Peripheral uptake of pHLIC in regions associated with acidosis in the LPS mouse (e.g. lung, liver, kidneys, and small intestine) could be predictive of neuroinflammation, which we observed as early as 12 h. The utility of our pHLIC probe to not only detect systemic but also CNS inflammation makes this approach attractive for investigating pH alterations in a vast number of applications, including stroke. Importantly, multiple novel therapeutics in development aim to treat metabolic acidosis by targeting ASICs (*42-45*). We posit that our radiotracer could monitor response to such therapies to improve clinical outcomes for those suffering from acidosis.

CONCLUSION

[^{64}Cu]Cu-c[E_4W_5C] pHLIC is a valuable tool to noninvasively and longitudinally demarcate the spatiotemporal evolution of acidosis in LPS-induced sepsis. Moreover, [^{64}Cu]Cu-c[E_4W_5C] has potential for broad application in other neuroinflammatory diseases. We expect that our pHLIC radiotracer will serve to increase understanding of the complex relationship between acidosis, immune function, and inflammation.

DISCLOSURES

J.S.L., O.A.A., and Y.K.R. are founders of pHLIP, Inc. They have shares in the company, but the company did not fund any part of the work reported in the paper, which was done in their academic laboratories. No other potential conflicts of interest (financial or otherwise) relevant to this article exist.

ACKNOWLEDGEMENTS

We gratefully acknowledge the Small Animal Imaging Core at MSK and Stanford University, and the Radiochemistry and Molecular Imaging Probe core (NIH grant P30 CA08748). We acknowledge the Center for Molecular Imaging and Nanotechnology (CMINT) Tow Fellowship through MSK (K.E.H.), financial support from NIH R35 CA232130-01A1 (J.S.L.), NIH R01 GM073857-09A1 (Y.K.R., O.A.A.) for pHLIP technologies, Chapman University School of Pharmacy for their core facility, and S.M.'s Ph.D. fellowship.

KEY POINTS

QUESTION: The *central hypothesis* of this study is that our pH low-insertion cyclic (pHLIC) peptide probe ([^{64}Cu]Cu-c[E_4W_5C]) will successfully demarcate acidosis in a mouse model of sepsis in a manner that correlates with ex vivo brain uptake and microglial/macrophage activation.

PERTINENT FINDINGS: We demonstrate that a pH-sensitive PET tracer detects acidosis in regions associated with sepsis-driven pro-inflammatory responses. We observed significantly increased ($P < 0.05$) uptake of [^{64}Cu]Cu-c[E_4W_5C] in the periphery and brain, which is mirrored by an increase in macrophage/microglial activation in these regions.

IMPLICATIONS FOR PATIENT CARE: [^{64}Cu]Cu-pHLIC is a valuable tool to noninvasively assess acidosis associated with both central and peripheral innate immune activation, and has potential to increase understanding of the dynamic relationship between acidosis and inflammation.

REFERENCES

1. Riemann A, Wußling H, Loppnow H, Fu H, Reime S, Thews O. Acidosis differently modulates the inflammatory program in monocytes and macrophages. Biochim Biophys Acta. 2016;1862(1):72-81.

2. Erra Díaz F, Dantas E, Geffner J. Unravelling the Interplay between Extracellular Acidosis and Immune Cells. Mediators Inflamm. 2018;2018:1218297.

3. Casimir GJ, Lefèvre N, Corazza F, Duchateau J, Chamekh M. The Acid-Base Balance and Gender in Inflammation: A Mini-Review. Front Immunol. 2018;9:475.

4. Wiederseiner J-M, Muser J, Lutz T, Hulter HN, Krapf R. Acute Metabolic Acidosis: Characterization and Diagnosis of the Disorder and the Plasma Potassium Response. J Am Soc Nephrol. 2004;15(6):1589-96.

5. Tyrtyshnaia AA, Lysenko LV, Madamba F, Manzhulo IV, Khotimchenko MY, Kleschevnikov AM. Acute neuroinflammation provokes intracellular acidification in mouse hippocampus. J Neuroinflammation. 2016;13:283.

6. Rajamäki K, Nordström T, Nurmi K, Åkerman KEO, Kovanen PT, Öörni K, Eklund KK. Extracellular acidosis is a novel danger signal alerting innate immunity via the NLRP3 inflammasome. J Biol Chem. 2013;288(19):13410-9.

7. Hoogland ICM, Houbolt C, van Westerloo DJ, van Gool WA, van de Beek D. Systemic inflammation and microglial activation: systematic review of animal experiments. J Neuroinflammation. 2015;12(1):114.

8. Wiederseiner J-M, Muser J, Lutz T, Hulter HN, Krapf R. Acute Metabolic Acidosis: Characterization and Diagnosis of the Disorder and the Plasma Potassium Response. J Am Soc Nephrol. 2004;15(6):1589-96.

9. Singh V, Khatana S, Gupta P. Blood gas analysis for bedside diagnosis. Natl J Maxillofac Surg. 2013;4(2):136-41.

10. Sood P, Paul G, Puri S. Interpretation of arterial blood gas. Indian J Crit Care Med. 2010;14(2):57-64.

11. de Nadai TR, de Nadai MN, Albuquerque AAS, de Carvalho MTM, Celotto AC, Evora PRB. Metabolic Acidosis Treatment as Part of a Strategy to Curb Inflammation. Int J Inflammation. 2013;2013:4.

12. Kraut JA, Madias NE. Metabolic acidosis: pathophysiology, diagnosis and management. Nat Rev Nephrol. 2010;6:274-285.

13. Rehncrona S. Brain acidosis. Ann Emerg Med. 1985;14(8):770-6.

14. Wyatt LC, Lewis JS, Andreev OA, Reshetnyak YK, Engelman DM. Applications of pHLIP Technology for Cancer Imaging and Therapy. Trends Biotechnol. 2017;35(7):653-64.

15. Wyatt LC, Moshnikova A, Crawford T, Engelman DM, Andreev OA, Reshetnyak YK. Peptides of pHLIP family for targeted intracellular and extracellular delivery of cargo molecules to tumors. PNAS. 2018;115(12):E2811.

16. Demoin DW, Wyatt LC, Edwards KJ, Abdel-Atti D, Sarparanta M, Pourat J, et al. PET Imaging of Extracellular pH in Tumors with (64)Cu- and (18)F-Labeled pHLIP Peptides: A Structure–Activity Optimization Study. Bioconjug Chem. 2016;27(9):2014-23.

17. Roberts S, Strome A, Choi C, Andreou C, Kossatz S, Brand C, et al. Acid specific dark quencher QC1 pHLIP for multi-spectral optoacoustic diagnoses of breast cancer. Sci Rep. 2019;9(1):8550.

18. John M, Vasso A, Eliada L, George D, Minos-Timotheos M, Maria K, Theodore T, Spyros D. Round and Round we Go: Cyclic Peptides in Disease. Curr Med Chem. 2006;13(19):2221-32.

19. Weerakkody D, Moshnikova A, El-Sayed NS, Adochite R-C, Slaybaugh G, Golijanin J, et al. Novel pH-Sensitive Cyclic Peptides. Sci Rep. 2016;6:31322.

20. Varatharaj A, Galea I. The blood-brain barrier in systemic inflammation. Brain, Behav Immun. 2017;60:1-12.

21. Gibot S, Buonsanti C, Massin F, Romano M, Kolopp-Sarda M-N, Benigni F, et al. Modulation of the triggering receptor expressed on the myeloid cell type 1 pathway in murine septic shock. Infect Immun. 2006;74(5):2823-30.

22. Allolio C, Magarkar A, Jurkiewicz P, Baxová K, Javanainen M, Mason PE, et al. Arginine-rich cell-penetrating peptides induce membrane multilamellarity and subsequently enter via formation of a fusion pore. PNAS. 2018;115(47):11923-8.

23. Waterhouse RN. Determination of lipophilicity and its use as a predictor of blood–brain barrier penetration of molecular imaging agents. Mol Imaging Biol. 2003;5(6):376-89.

24. Wei L, Easmon J, Nagi RK, Muegge BD, Meyer LA, Lewis JS. 64Cu-Azabicyclo[3.2.2]Nonane Thiosemicarbazone Complexes: Radiopharmaceuticals for PET of Topoisomerase II Expression in Tumors. J Nucl Med. 2006;47(12):2034-41.

25. Chaney AM, Johnson EM, Cropper HC, James ML. PET Imaging of Neuroinflammation Using [11C]DPA-713 in a Mouse Model of Ischemic Stroke. JoVE. 2018(136):57243.

26. James ML, Shen B, Zavaleta CL, Nielsen CH, Mesangeau C, Vuppala PK, et al. New positron emission tomography (PET) radioligand for imaging σ-1 receptors in living subjects. J Med Chem. 2012;55(19):8272-82.

27. James ML, Belichenko NP, Shuhendler AJ, Hoehne A, Andrews LE, Condon C, et al. [(18)F]GE-180 PET Detects Reduced Microglia Activation After LM11A-31 Therapy in a Mouse Model of Alzheimer's Disease. Theranostics. 2017;7(6):1422-36.

28. Lively S, Schlichter LC. Microglia Responses to Pro-inflammatory Stimuli (LPS, IFNγ+TNFα) and Reprogramming by Resolving Cytokines (IL-4, IL-10). Front Cell Neurosci. 2018;12:215.

29. Furube E, Kawai S, Inagaki H, Takagi S, Miyata S. Brain Region-dependent Heterogeneity and Dose-dependent Difference in Transient Microglia Population Increase during Lipopolysaccharide-induced Inflammation. Sci Rep. 2018;8(1):2203.

30. Semmler A, Okulla T, Sastre M, Dumitrescu-Ozimek L, Heneka MT. Systemic inflammation induces apoptosis with variable vulnerability of different brain regions. J Chem Neuroanat. 2005;30(2):144-57.

31. Okuyama S, Makihata N, Yoshimura M, Amakura Y, Yoshida T, Nakajima M, Furukawa Y. Oenothein B suppresses lipopolysaccharide (LPS)-induced inflammation in the mouse brain. Int J Mol Sci. 2013;14(5):9767-78.

32. Skelly DT, Hennessy E, Dansereau MA, Cunningham C. A systematic analysis of the peripheral and CNS effects of systemic LPS, IL-1beta, TNF-alpha and IL-6 challenges in C57BL/6 mice. PLoS One. 2013;8(7):e69123-43.

33. Bennett ML, Bennett FC, Liddelow SA, Ajami B, Zamanian JL, Fernhoff NB, et al. New tools for studying microglia in the mouse and human CNS. PNAS. 2016;113(12):E1738-E46.

34. Zhang X, Dong H, Zhang S, Lu S, Sun J, Qian Y. Enhancement of LPS-Induced Microglial Inflammation Response via TLR4 Under High Glucose Conditions. Cell Physiol Biochem. 2015;35(4):1571-81.

35. Catorce MN, Gevorkian G. LPS-induced Murine Neuroinflammation Model: Main Features and Suitability for Pre-clinical Assessment of Nutraceuticals. Curr Neuropharmacol. 2016;14(2):155-64.

36. Chen LQ, Randtke EA, Jones KM, Moon BF, Howison CM, Pagel MD. Evaluations of Tumor Acidosis Within In Vivo Tumor Models Using Parametric Maps Generated with Acido CEST MRI. Mol Imaging Biol. 2015;17(4):488-96.

37. Jones KM, Pollard AC, Pagel MD. Clinical applications of chemical exchange saturation transfer (CEST) MRI. J Mag Res Imaging. 2018;47(1):11-27.

38. Longo DL, Bartoli A, Consolino L, Bardini P, Arena F, Schwaiger M, Aime S. In Vivo Imaging of Tumor Metabolism and Acidosis by Combining PET and MRI-CEST pH Imaging. Cancer Res. 2016;76(22):6463-70.

39. Gallagher FA, Kettunen MI, Brindle KM. Imaging pH with hyperpolarized 13C. NMR Biomed. 2011;24(8):1006-15.

40. Guglielmetti C, Najac C, Didonna A, Van der Linden A, Ronen SM, Chaumeil MM. Hyperpolarized ^{13}C MR metabolic imaging can detect neuroinflammation in vivo in a multiple sclerosis murine model. PNAS. 2017;114(33):E6982-91.

41. Scheiner B, Lindner G, Reiberger T, Schneeweiss B, Trauner M, Zauner C, Funk G-C. Acid-base disorders in liver disease. J Hepatol. 2017;67(5):1062-73.

42. Ortega-Ramírez A, Vega R, Soto E. Acid-Sensing Ion Channels as Potential Therapeutic Targets in Neurodegeneration and Neuroinflammation. Mediators Inflamm. 2017;2017:3728096.

43. Brown D, Melamed ML. New Frontiers in Treating Uremic Metabolic Acidosis. Clin J Am Soc Nephrol. 2018;13(1):4-5.

44. Kraut JA, Raphael KL. Drug removal of gastric acid: a novel treatment of metabolic acidosis. The Lancet. 2019;394(10196):363-4.

45. Zhou R-P, Wu X-S, Wang Z-S, Xie Y-Y, Ge J-F, Chen F-H. Novel Insights into Acid-Sensing Ion Channels: Implications for Degenerative Diseases. Aging Dis. 2015;7(4):491-501.

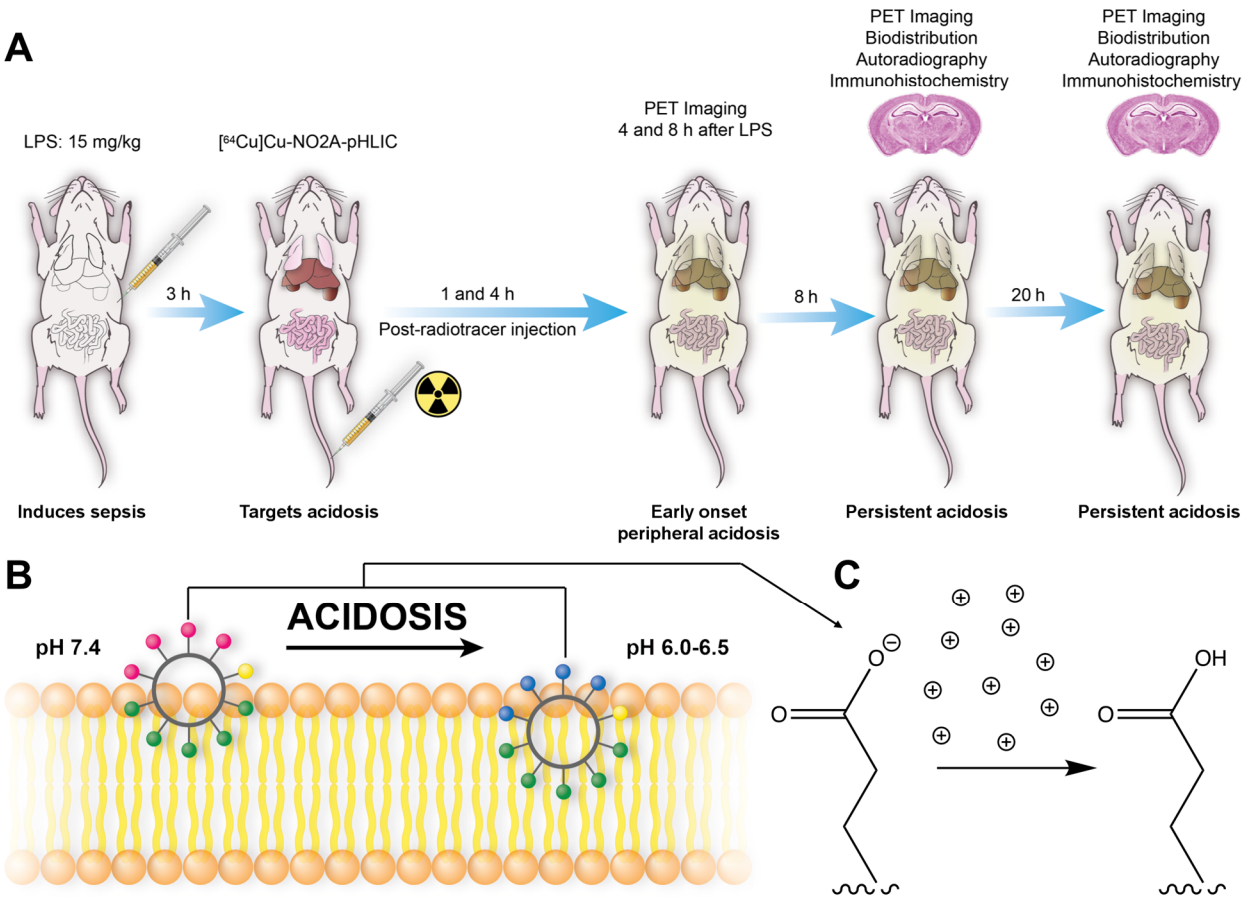

FIGURE 1. Study workflow and mechanism of pHLIC membrane insertion. (A) LPS was injected i.p. into C57BL/6J mice and ^{64}Cu-labelled pHLIC radiotracer was administered intravenously 3 h later. Mice underwent PET imaging at 4, 8, 12, and 24 h post-LPS treatment. Autoradiography and immunohistochemistry were performed 12 and 24 h post-LPS treatment. (B) pHLICs consist of negatively charged glutamate residues located at one side of the cycle and hydrophobic tryptophan residues on the other. Pink circles represent glutamate residues, which become blue upon protonation as they insert into the membrane. Green circles represent tryptophan residues, and yellow circle is the cysteine residue (point of conjugation the NO2A chelator to enable ^{64}Cu-labeling). (C) Example protonation of glutamate residues in the acidic microenvironment.

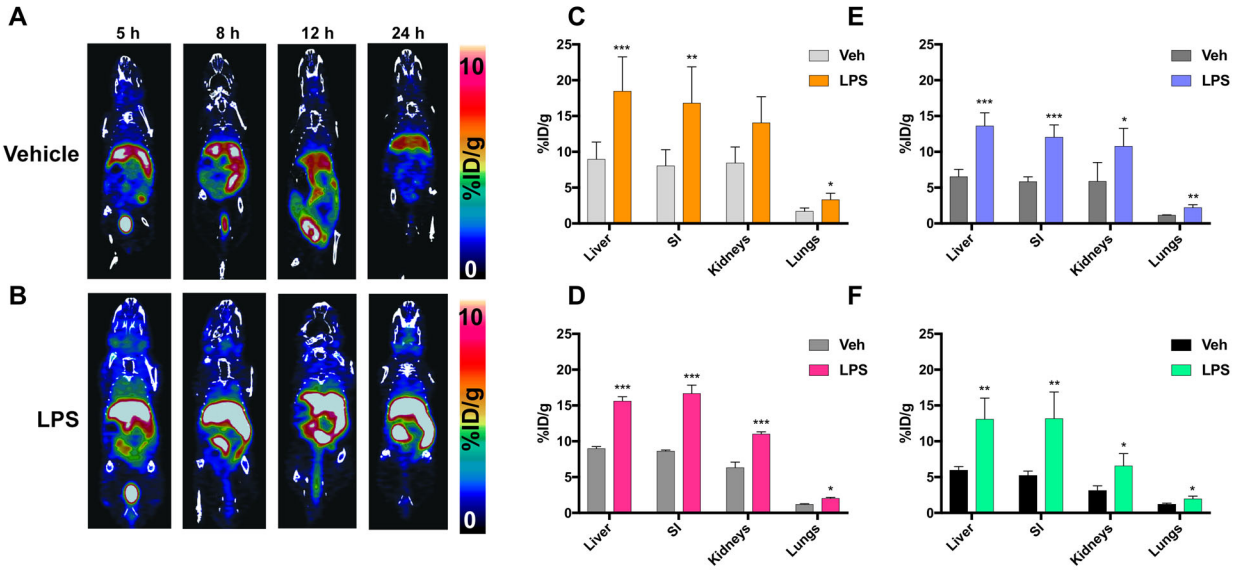

FIGURE 2. [^{64}Cu]Cu-c[E$_4$W$_5$C] pHLIC detects the presence of acidosis via serial PET imaging. (A) PET images of vehicle-treated vs. (B) LPS-treated mice and quantitation at 4 h (C), 8 h (D), 12 h (E), and 24 h (F) post-LPS treatment. Data is represented as average %ID/g ± SD (*n* = 4 animals/group).[†]

In order to help clarify studies done between institutions, figures and tables marked with a diesis ([†]) were done at Stanford and those marked with a double diesis ([‡]) were done at MSK.

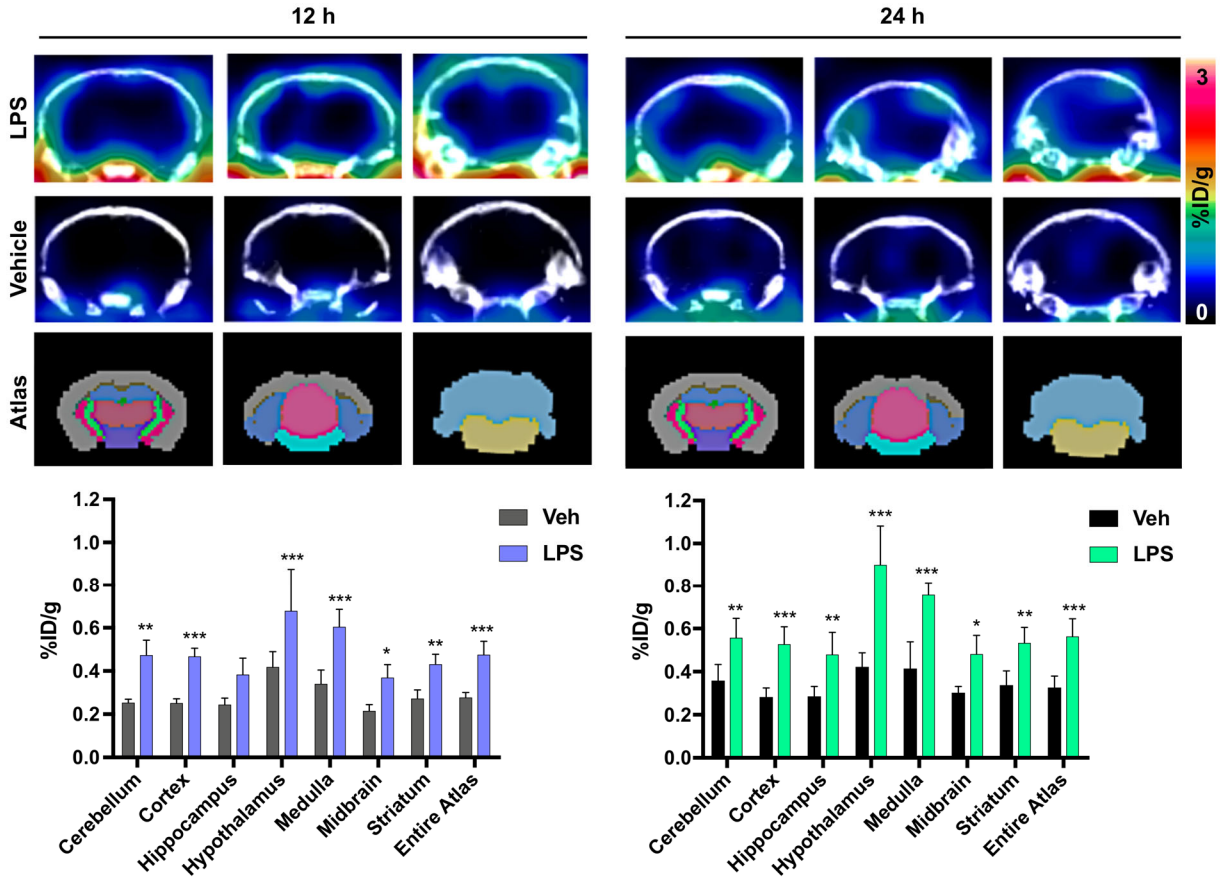

FIGURE 3. Representative coronal brain PET/CT images of [^{64}Cu]Cu-c[E_4W_5C] uptake and brain-atlas guided PET quantitation of vehicle vs. LPS-treated mice 12 and 24 h after tracer injection. Data represented as average %ID/g ± SD (*n* = 4 animals/group).†

In order to help clarify studies done between institutions, figures and tables marked with a diesis (†) were done at Stanford and those marked with a double diesis (‡) were done at MSK.

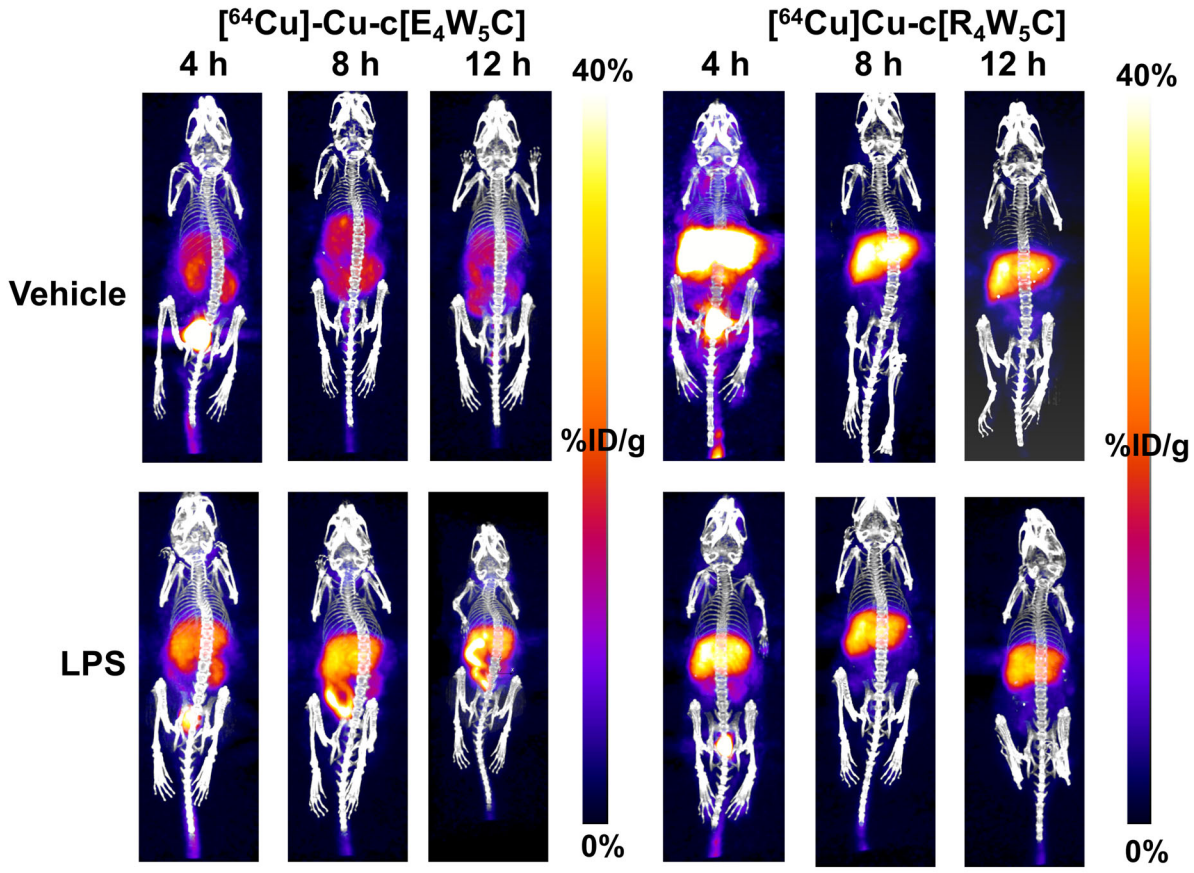

FIGURE 4. Serial [^{64}Cu]Cu-c[E$_4$W$_5$C] and [^{64}Cu]Cu-c[R$_4$W$_5$C] (control) PET highlights the specificity of pHLIC for acidosis in LPS-induced mice over 12 h. Data represented as average %ID/g ± SD (*n* = 4 animals/group).‡

In order to help clarify studies done between institutions, figures and tables marked with a diesis (†) were done at Stanford and those marked with a double diesis (‡) were done at MSK.

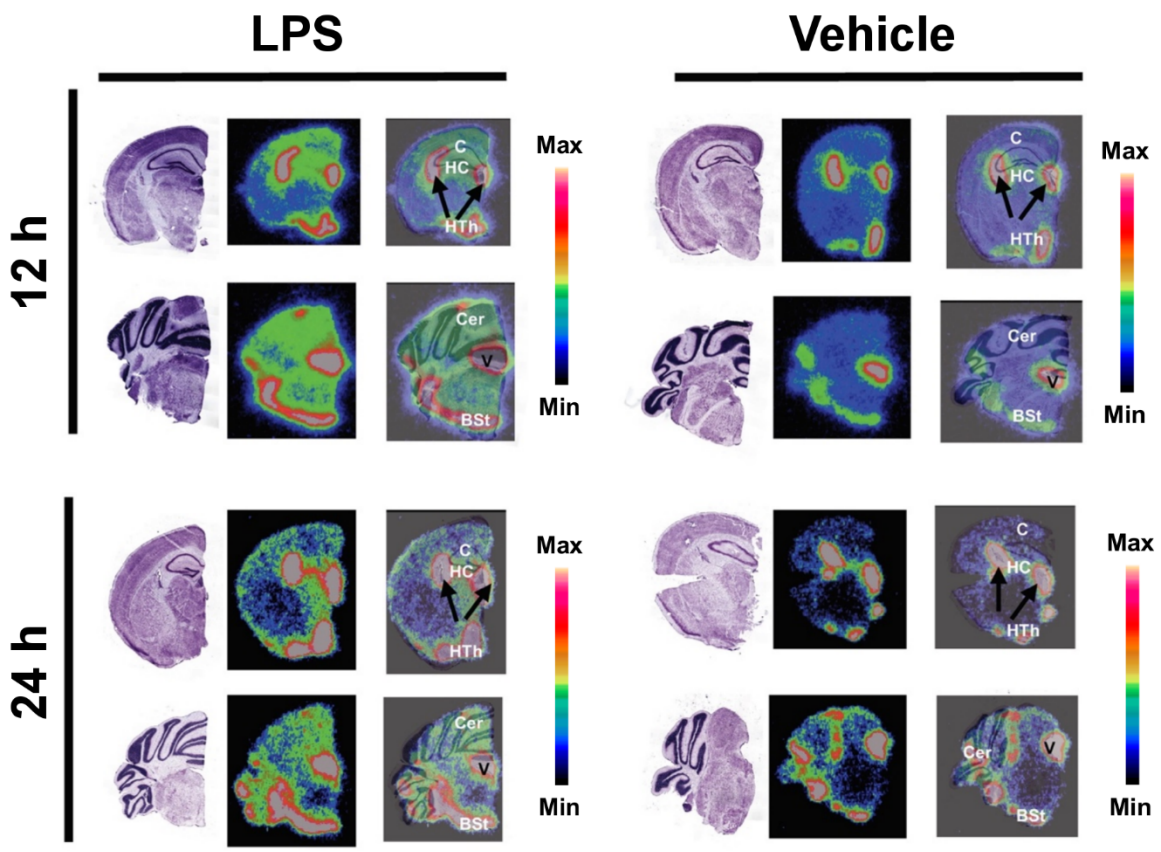

FIGURE 5. Autoradiography and nissl staining enables high-resolution detection of [^{64}Cu]Cu-c[E_4W_5C] uptake in brain slices. Cer: cerebellum; C: Cortex; HC: Hippocampus; Hth: Hypothalamus; BSt: brain stem; V: ventricle. Data represented show *n* = 3 animals/group.†

In order to help clarify studies done between institutions, figures and tables marked with a diesis (†) were done at Stanford and those marked with a double diesis (‡) were done at MSK.

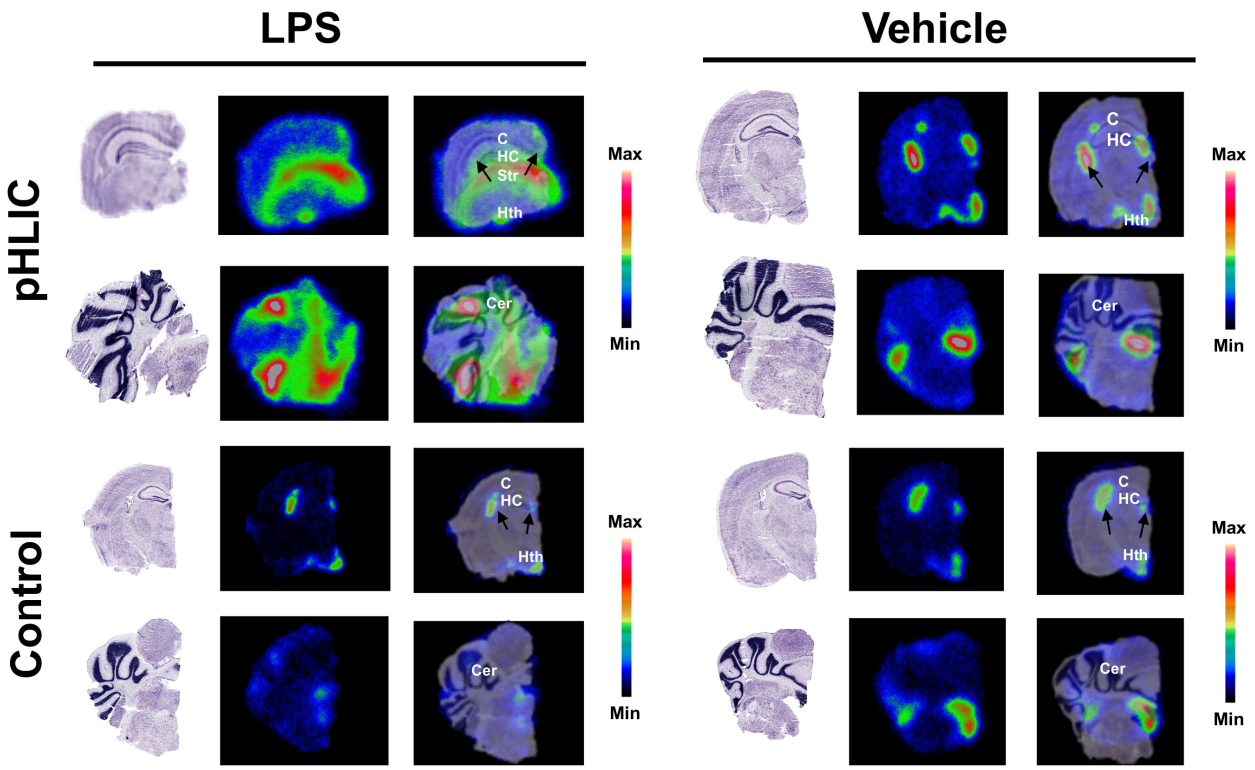

FIGURE 6. Autoradiography verifies specificity of [^{64}Cu]Cu-c[E_4W_5C] uptake (top) vs. [^{64}Cu]Cu-c[R_4W_5C] control (bottom) in brain slices 24 h post-LPS administration. Cer: cerebellum; C: Cortex; HC: Hippocampus; Hth: Hypothalamus; Str: striatum. Data represented show groups of vehicle: *n* = 3 animals/group and LPS: *n* = 2 animals/group.‡

In order to help clarify studies done between institutions, figures and tables marked with a diesis (†) were done at Stanford and those marked with a double diesis (‡) were done at MSK.

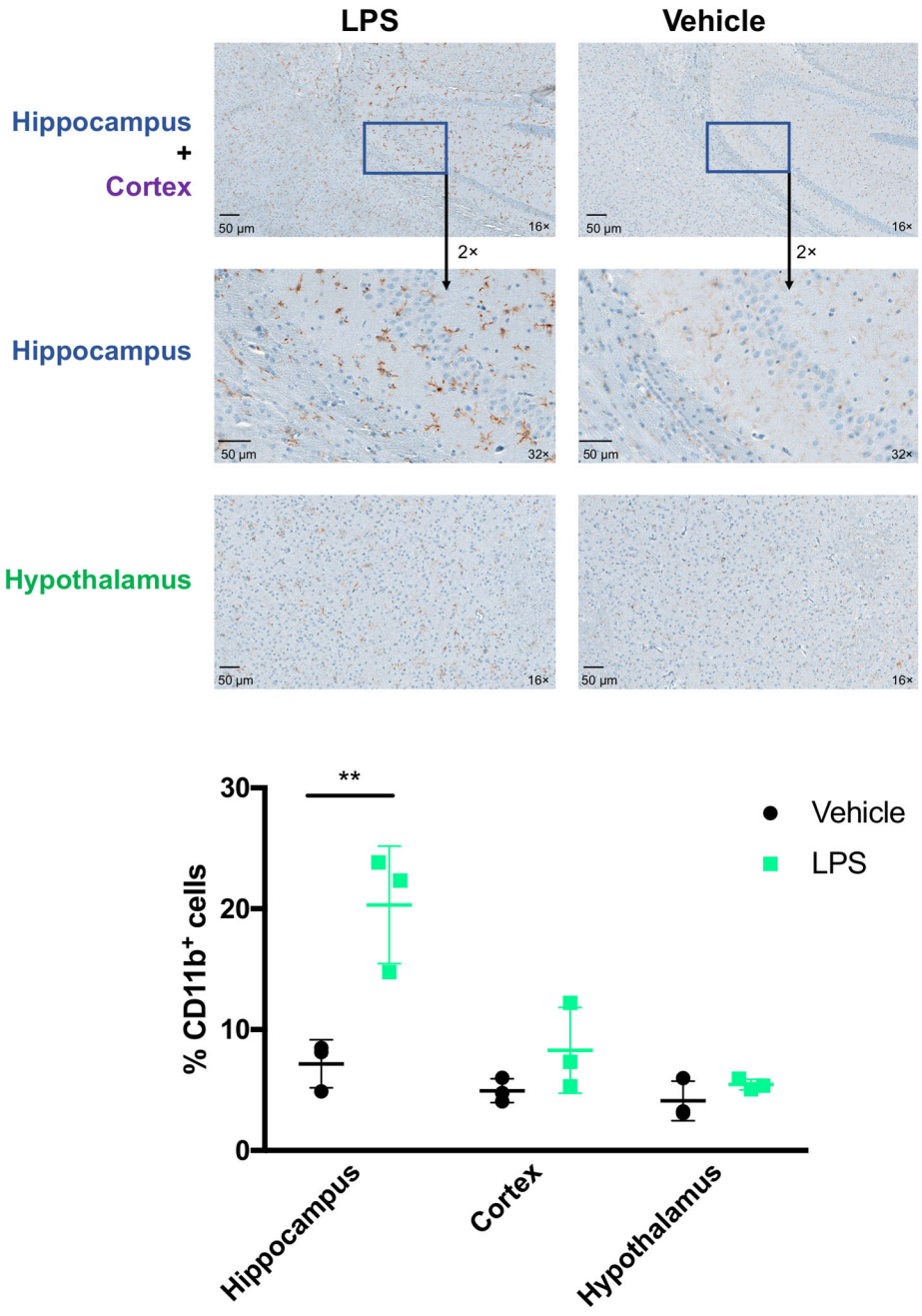

FIGURE 7. Immunohistochemical staining of CD11b identifies increased microglia/macrophages in select brain regions of LPS-treated compared to vehicle-treated mice. Data represented as average %ID/g ± SD (*n* = 3 animals/group).‡

In order to help clarify studies done between institutions, figures and tables marked with a diesis (†) were done at Stanford and those marked with a double diesis (‡) were done at MSK.

Title: Demarcation of Sepsis-Induced Peripheral and Central Acidosis with pH-Low Insertion Cyclic (pHLIC) Peptide

Running title: Tracking Acidosis Using pH-Targeted PET

Supplemental Information

Authors and Affiliations: Kelly E. Henry,[1] Aisling M. Chaney,[2] Veronica L. Nagle,[1,3,4] Haley C. Cropper,[2] Saghar Mozaffari,[5] Keykavous Parang,[5] Gregory Slaybaugh,[6] Oleg A. Andreev,[6] Yana K. Reshetnyak,[6] Michelle L. James,[2,7*] Jason S. Lewis[1,3,4,8*]

[1]Department of Radiology, Memorial Sloan Kettering Cancer Center, New York, NY

[2]Department of Radiology, Stanford University, Stanford, CA

[3]Molecular Pharmacology Program, Memorial Sloan Kettering Cancer Center, New York, NY

[4]Departments of Pharmacology and Radiology, Weill Cornell Medical College, New York, NY

[5]Center for Targeted Drug Delivery, Department of Biomedical and Pharmaceutical Sciences, Chapman University School of Pharmacy, Irvine, CA

[6]Department of Physics, University of Rhode Island, Kingston, RI

[7]Department of Neurology & Neurological Science, Stanford University, Stanford, CA

[8]Radiochemistry and Molecular Imaging Probes Core, Memorial Sloan Kettering Cancer Center, New York, NY

M.L.J. -- mljames@stanford.edu, P: 650-497-0153; F: 650-724-4948 *Co-corresponding author

J.S.L. -- lewisj2@mskcc.org, P: 646-888-3038, F: 646-888-3059, *Co-corresponding author

K.E.H. -- henryk1@mskcc.org, P: 646-888-3271, F: 646-888-3059, Chief Postdoctoral Research Fellow

FINANCIAL SUPPORT.

We gratefully acknowledge the Small Animal Imaging Core at MSK and Stanford University, and the Radiochemistry and Molecular Imaging Probe core (NIH grant P30 CA08748). We acknowledge the Center for Molecular Imaging and Nanotechnology (CMINT) Tow Fellowship through MSK (K.E.H.), financial support from NIH R35 CA232130-01A1 (J.S.L.), NIH R01 GM073857-09A1 (Y.K.R., O.A.A.) for pHLIP technologies, Chapman University School of Pharmacy for their core facility, and S.M.'s Ph.D. fellowship.

Disclaimer of Variability Between Institutions.

†Indicates experiments done at Stanford University. Anesthesia supplement for in vivo experiments was pure oxygen, resulting in lower baseline uptake for all radiotracers.

‡Indicates experiments done at MSK. Anesthesia supplement for in vivo experiments was medical air, resulting in slightly hypoxic conditions and higher baseline uptake for all radiotracers.

†‡Indicates experiments done at both Stanford and MSK, with average data pooled.

In the spirit of full transparency, we have included all data done at Stanford and MSK and indicate where the data was collected to make our multi-institutional collaboration extremely clear for the reader. We have included thorough statistical analysis of not only vehicle vs. LPS groups for both pHLIC and control radiotracers, but also uptake of the pHLIC vs. control radiotracer between LPS groups. The key result highlighting the difference between LPS groups is represented in the ex vivo biodistribution at 24 h (Supplemental Fig. 18 and Supplemental Table 8), coupled to the autoradiography (Fig. 6) at 24 h and serves as an appropriate demonstration of specificity for the acid-sensitive radiotracer [^{64}Cu]Cu-NO2A-c[E_4W_5C]. We show significantly higher uptake with our pHLIC radiotracer in the brain compared to our [^{64}Cu]Cu-NO2A-c[R_4W_5C] control. Additionally, our biophysical measurements (Supplemental Fig. 6) indicate the pH-sensitivity of the pHLIC (^{nat}Cu-NO2A-c[E_4W_5C] vs. non-acid-sensitive control (^{nat}Cu-NO2A-c[R_4W_5C]), further supporting the specificity of our pHLIC tracer for acidosis. We hope the discrepancy in baseline uptake of tracer between institutions (albeit similar trends and statistics between vehicle and LPS groups) will serve as a reminder to the nuclear medicine field how anesthesia and oxygen content can significantly change radiotracer uptake, especially with radiotracers that cross the BBB. We hold ourselves and the rest of the community to the highest standards and demonstrate the need for rigor and reproducibility among multi-institutional collaborations.

*See references 2-6 for how oxygen and anesthesia time can affect cerebral blood flow and radiotracer uptake, particularly in neuroimaging.

Materials and Methods.

Synthesis and purification of pHLIC-NO2A Constructs. Cyclic peptides c[E_4W_5C] or c[R_4W_5C] (1 mg, 0.6-0.65 μmol) was mixed with 2× stoichiometric excess NO2A-maleimide (1.2-1.3 μmol) in a 90:10 mixture of anhydrous dimethylformamide (DMF):degassed phosphate-buffered saline (PBS) for 2 h at 37 °C. The conjugate was purified using C_{18} Preparative-HPLC with a 5-95% acetonitrile with 0.1% TFA over 40 min gradient (t_R = 25 min) and evaluated using matrix assisted light desorption-ionization time-of-flight mass spectrometry (MALDI-ToF) or liquid chromatography mass spectrometry (LCMS). Two additional peptides (another cyclic "pHLIC" variant and one linear "pHLIP") were also conjugated to NO2A-maleimide using similar methods.

Cold labeling of c[E_4W_5C] and c[R_4W_5C]. pHLIC-NO2A conjugates (20 μL, 16 nmol) was diluted in 0.1 M NH_4Ac (pH 5.5) and incubated with a 2× stoichiometric excess of $^{nat}CuCl_2$ at 80 °C for 15 min. ^{nat}Cu-c[E_4W_5C] ^{nat}Cu-c[R_4W_5C] were purified using a C_{18} Sep Pak with fractionated elutions of 100% ethanol. Fractions were validated for successful labeling and purity via LCMS, then pooled and lyophilized and sent to URI for biophysical measurements.

Biophysical Studies.

Liposome Preparation. Large unilamellar vesicles (LUVs) were prepared by extrusion. POPC (1-palmitoyl-2-oleoyl-sn-glycero-3-phosphocholine, Avanti Polar Lipids) were dissolved in chloroform, desolvated on a rotary evaporator, and left under high vacuum for several hours. The phospholipid film was then rehydrated in 10 mM phosphate buffer pH 8.0, the lipid bilayer was gently dissolved, and extruded 21 times through the membranes with 50 nm pore sizes to obtain LUVs.

Steady-State Fluorescence. Freshly prepared peptides and POPC vesicles were mixed to have 3 μM of a peptide and 0.6 mM of lipids in the final solution. Steady-state fluorescence measurements were carried out on a PC1 spectrofluorometer (ISS, Inc.) under temperature control at 25 °C. Fluorescence was excited at 280 nm and recorded with the excitation and emission slits set at 4 nm. The polarizers

in the excitation and emission paths were set at the “magic” angle (54.7° from the vertical orientation) and vertically (0°), respectively.

***pH-Dependence*.** pH-dependent partitioning of the constructs into a lipid bilayer of the membrane was examined by the shift of the position of the fluorescence spectral maximum for the constructs in the presence of POPC liposomes induced by a drop of pH from 7.4 to 4 by the addition of HCl. The constructs were incubated overnight with 50-nm POPC liposomes (final concentration of the peptides and POPC in solution was 3 μM and 0.6 mM, respectively), and pH decrease was achieved by the addition of aliquots of 0.5 and 0.1 M HCl. pH was measured by micro-electrode probe (Thermo Electron Corporation, Orion Ross Micro pH electrode). Fluorescence spectra were recorded at each pH value. The spectra were analyzed by the decomposition algorithms using Protein Fluorescence and Structural Toolkit (PFAST) toolkit to establish the position of the emission maximum (*1*). Finally, the positions of the fluorescence spectral maxima (λ_{max}) were plotted versus pH, and the Henderson–Hasselbalch equation was used to fit the data (using Origin 9.0 software):

$$\lambda_{max} = \lambda_1 + \frac{\lambda_1 - \lambda_2}{1 + 10^{(pH-pK)}}$$

where λ_1 and λ_2 are the beginning and the end of the transition, respectively, and *pK* – is the midpoint of the transition.

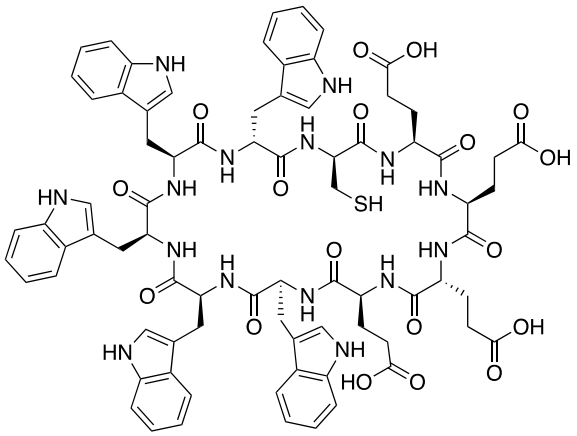

c[E_4W_5C]
Chemical Formula: $C_{78}H_{83}N_{15}O_{18}S$
Molecular Weight: 1550.67

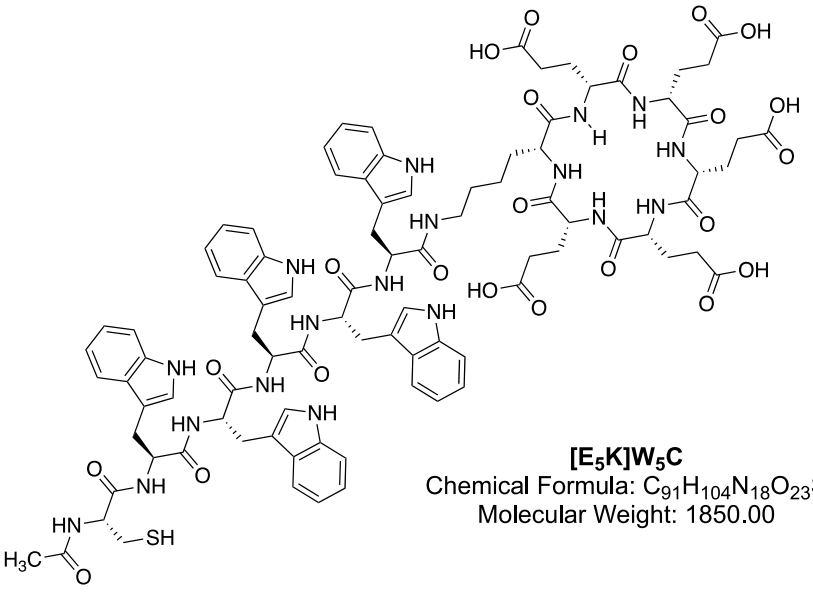

[E_5K]W_5C
Chemical Formula: $C_{91}H_{104}N_{18}O_{23}S$
Molecular Weight: 1850.00

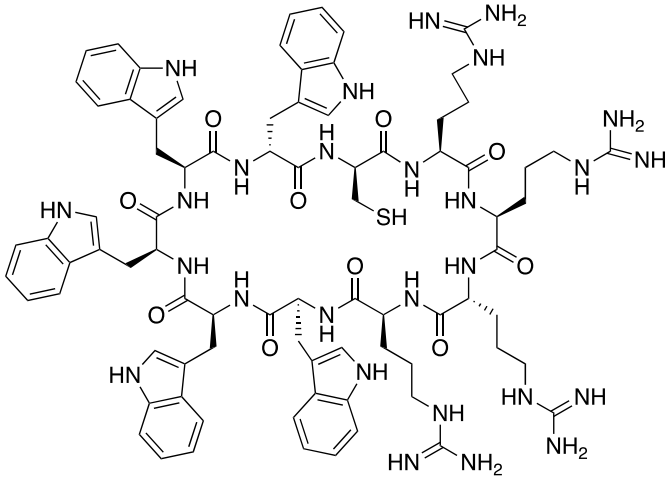

c[R_4W_5C]
Chemical Formula: $C_{82}H_{103}N_{27}O_{10}S$
Molecular Weight: 1658.97

Sequence: GCDNNEGFFATLGGEIPLWSDVVLAIEG
pHLIP-HM2A
Chemical Formula: $C_{131}H_{195}N_{31}O_{43}$
Molecular Weight: 2924.19

Supplemental Fig. 1. Sequence and structure of pHLIP and pHLIC peptides.

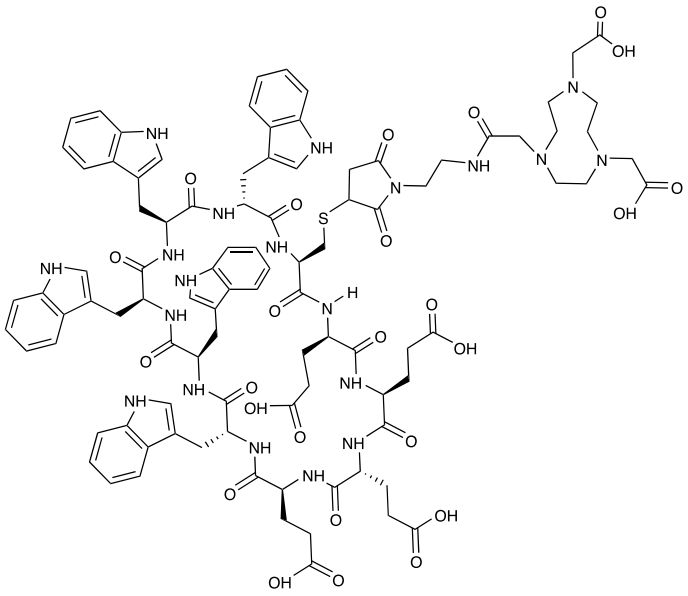

c[E_4W_5C]-NO2A
Chemical Formula: $C_{96}H_{110}N_{20}O_{25}S$
Molecular Weight: 1976.11

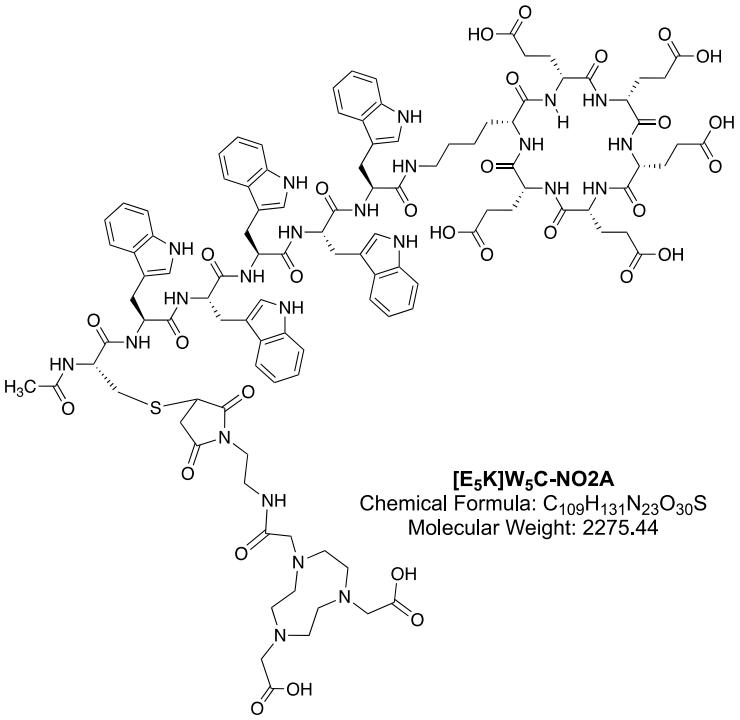

[E_5K]W_5C-NO2A
Chemical Formula: $C_{109}H_{131}N_{23}O_{30}S$
Molecular Weight: 2275.44

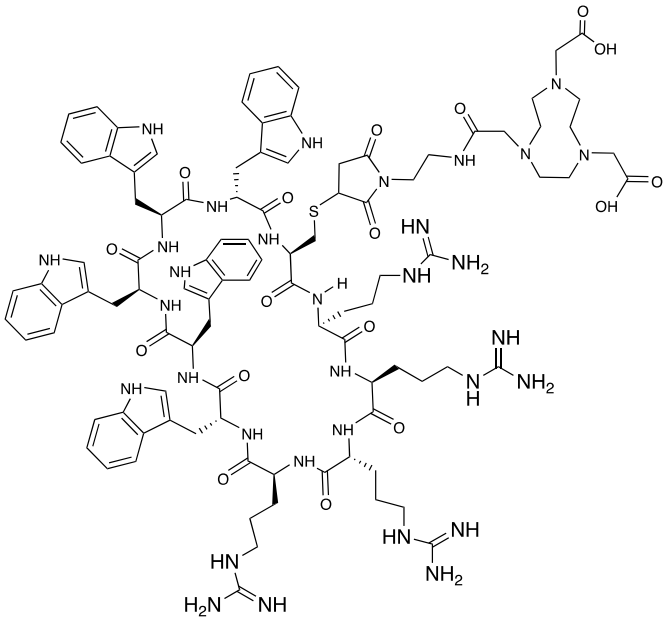

c[R_4W_5C]-NO2A
Chemical Formula: $C_{100}H_{130}N_{32}O_{17}S$
Molecular Weight: 2084.41

Supplemental Fig. 2. Structure of pHLIC-NO2A peptide conjugates.

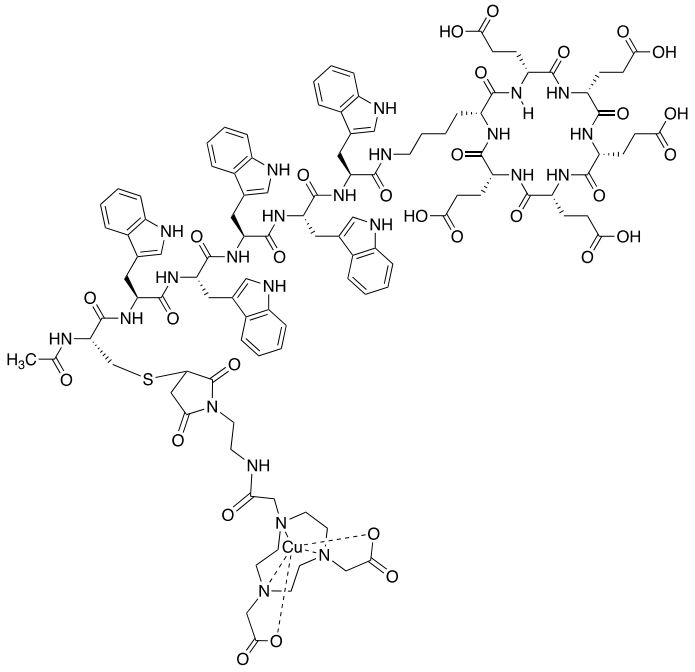

[^{64}Cu]Cu-NO2A-[E$_5$K]W$_5$C

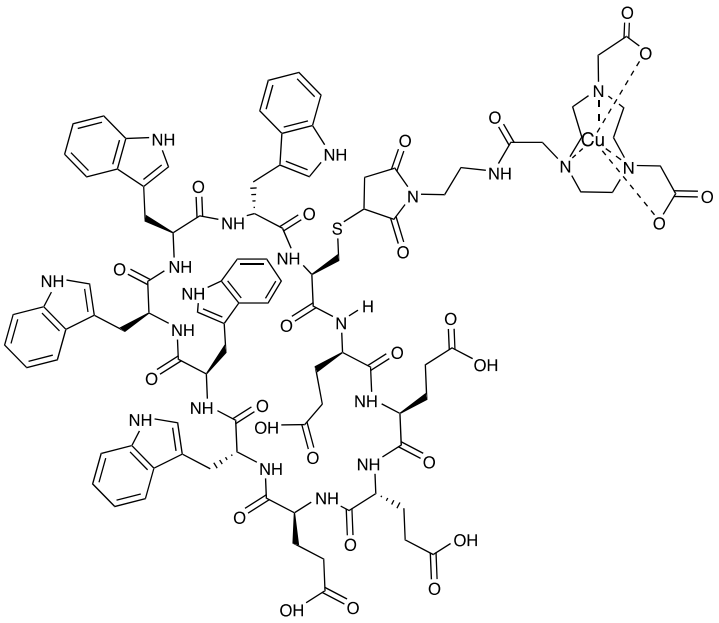

[^{64}Cu]Cu-NO2A-c[E$_4$W$_5$C]

[^{64}Cu]Cu-NO2A-c[E$_4$W$_5$C]

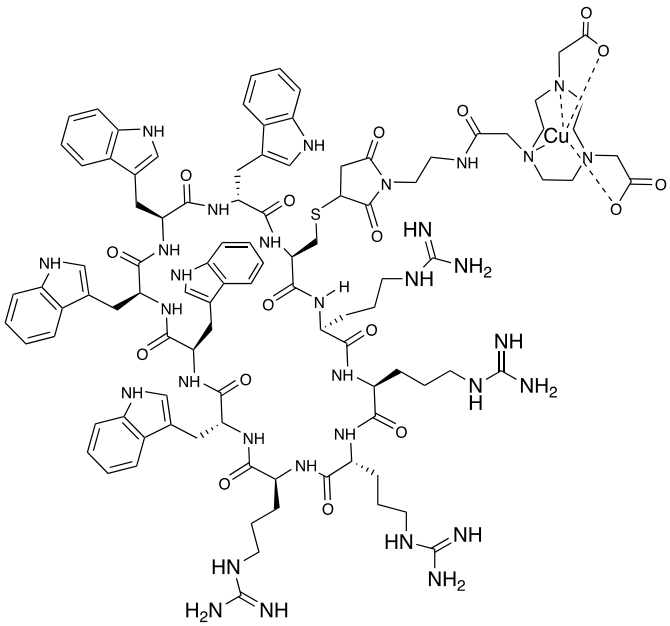

[^{64}Cu]Cu-NO2A-c[R$_4$W$_5$C]

Supplemental Fig. 3. Structure of ^{64}Cu-labelled pHLIC-NO2A peptide conjugates.

‡**Supplemental Fig. 4**. Instant thin-layer chromatography quality control of all ^{64}Cu-labelled pHLIC/pHLIP radiotracers.

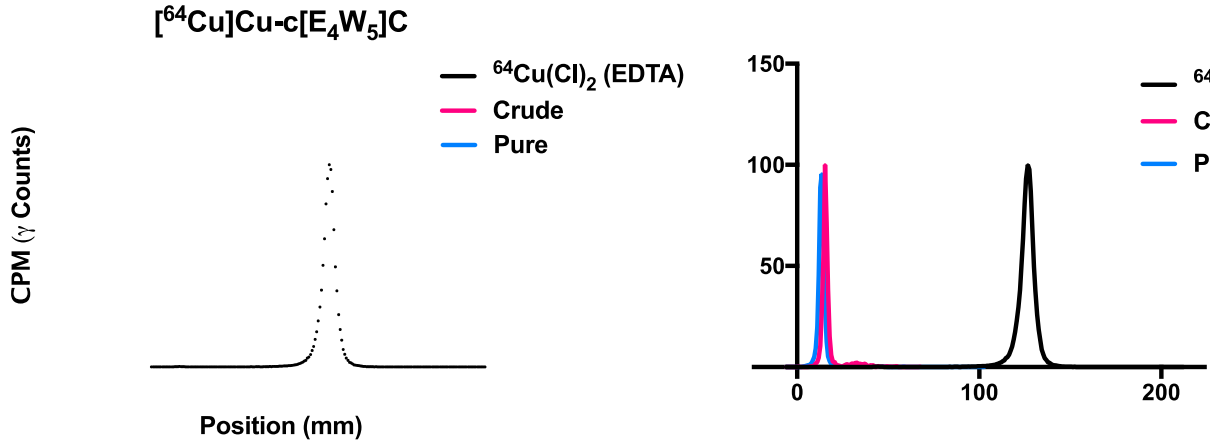

‡**Supplemental Table 1**. Experimentally determined LogP values of ^{64}Cu-labelled pHLIC/pHLIP radiotracers.

Compound	LogD (pH 6)			LogD (pH 7.4)		
[^{64}Cu]Cu-HM2A	-1.9	±	0.1	-2.2	±	0.3
[^{64}Cu]Cu-c[E_4W_5C]	2.5	±	0.1	2	±	0.2
[^{64}Cu]Cu-[E_5K]W_5C	2.1	±	0.1	2.3	±	0.3

‡**Supplemental Fig. 5**. Serum stability of ^{64}Cu-labelled pHLIC radiotracers (*n* = 3).

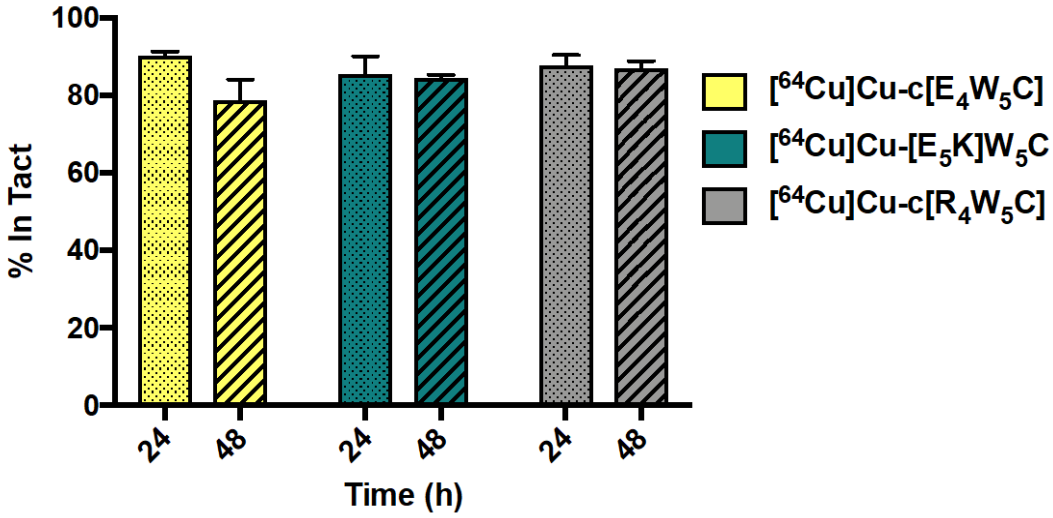

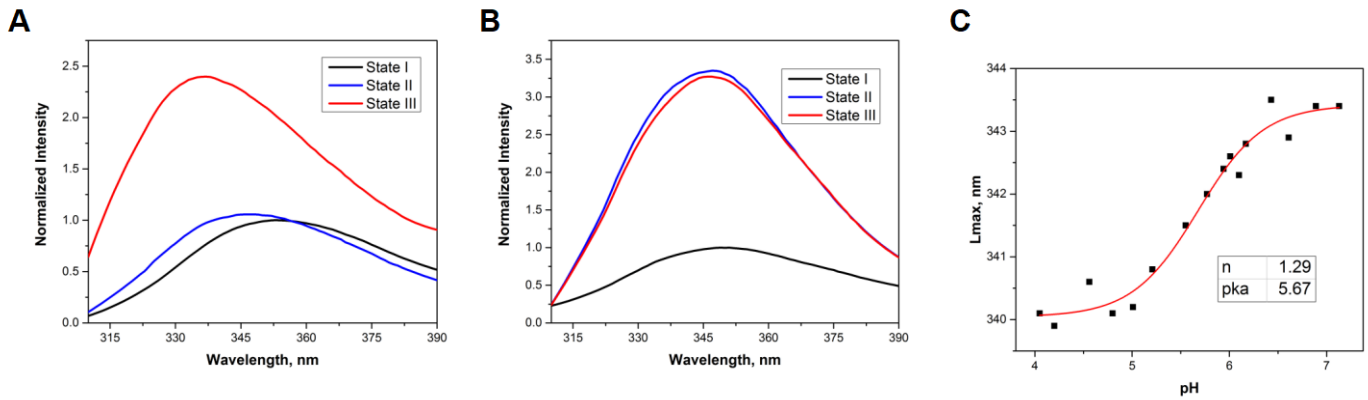

Supplemental Fig. 6. Tryptophan fluorescence spectra are shown from [^{nat}Cu]Cu-c[E_4W_5C] (A) and [^{nat}Cu]Cu-c[R_4W_5C] (B) in aqueous solution at pH 8 (black lines), at pH 8 in the presence of POPC liposomes (blue lines) and at pH 4 in the presence of POPC liposomes (red lines). The pH-dependent partition of [^{nat}Cu]Cu-c[E_4W_5C] into the lipid bilayers of POPC liposomes was studied by monitoring the changes in the position of maxima of fluorescence spectra as function of pH (C). The data were fitted using the Henderson-Hasselbalch equation, the fitting curves and 95% confidence interval are shown by red and pink areas, respectively.

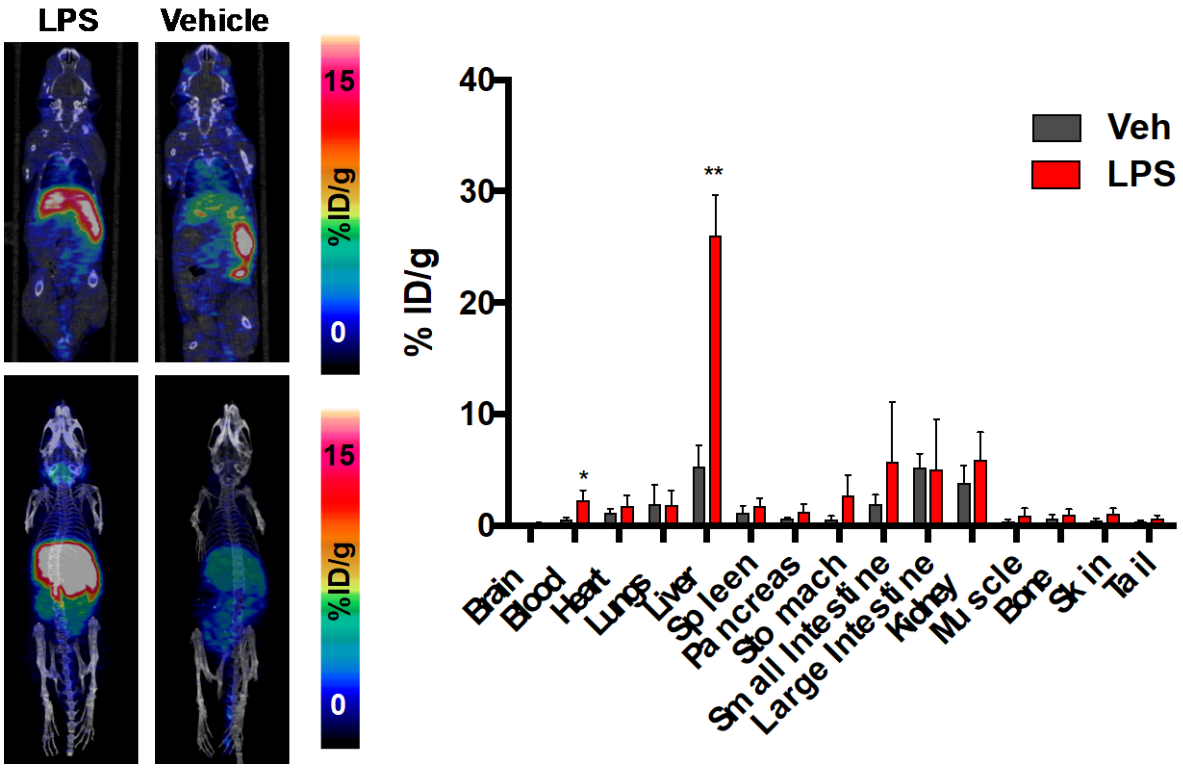

†**Supplemental Fig. 7**. PET imaging of [^{64}Cu]Cu-[E$_5$K]W$_5$C peptide and corresponding biodistribution at 24 h. The top panel represents coronal slices of the mice and the bottom panel represents the maximum intensity projections (MIPs). Data is represented as average %ID/g ± SD with *n* = 3-4 animals/group.

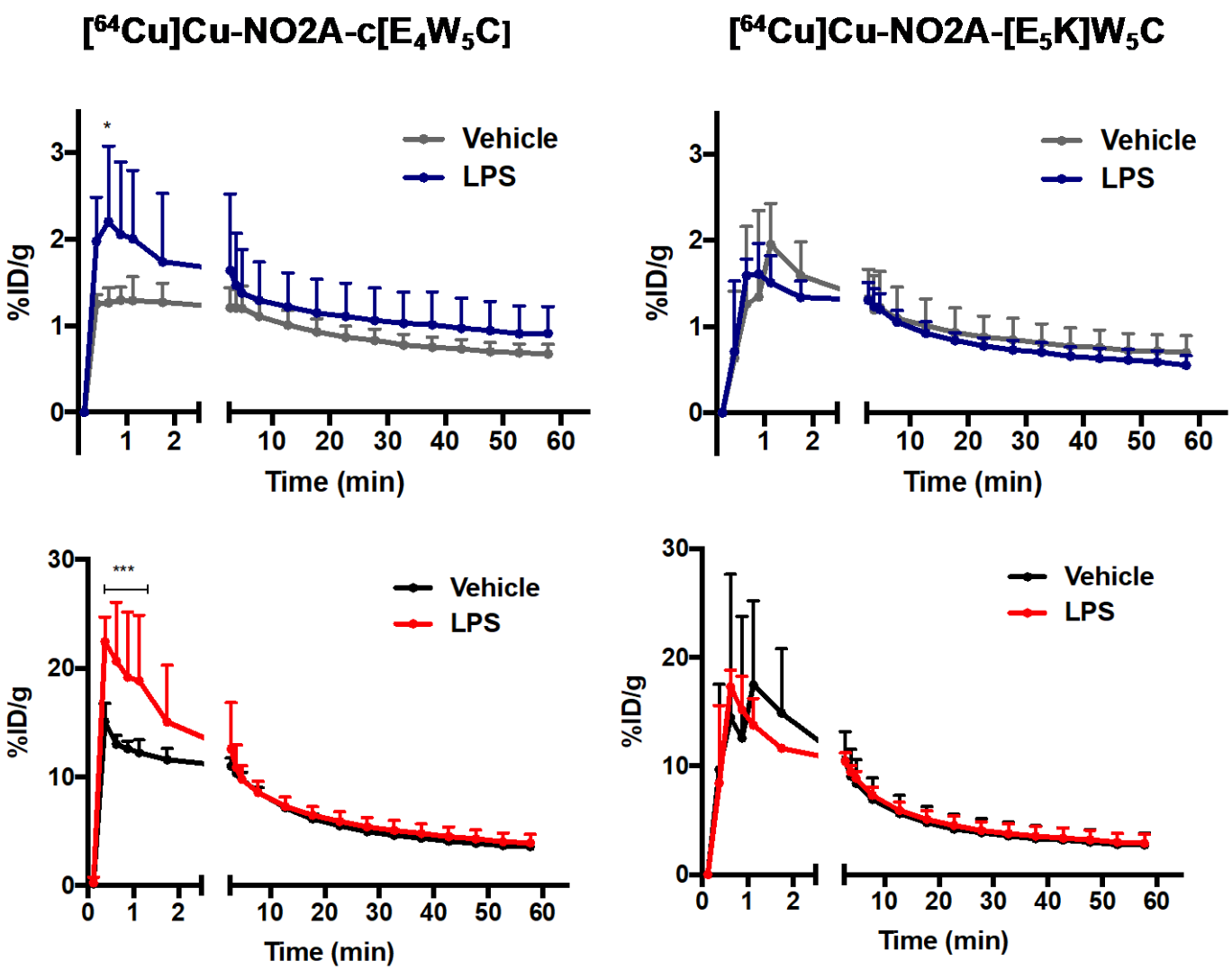

†**Supplemental Fig. 8**. Dynamic PET quantitation for the blood (top figures, red and black) and brain (bottom figures, blue and gray) uptake [^{64}Cu]Cu-NO2A-c[E$_4$W$_5$C] and [^{64}Cu]Cu-NO2A-[E$_5$K]W$_5$C pHLIC peptides. Data is represented as average %ID/g ± SD with *n* = 4 animals/group.

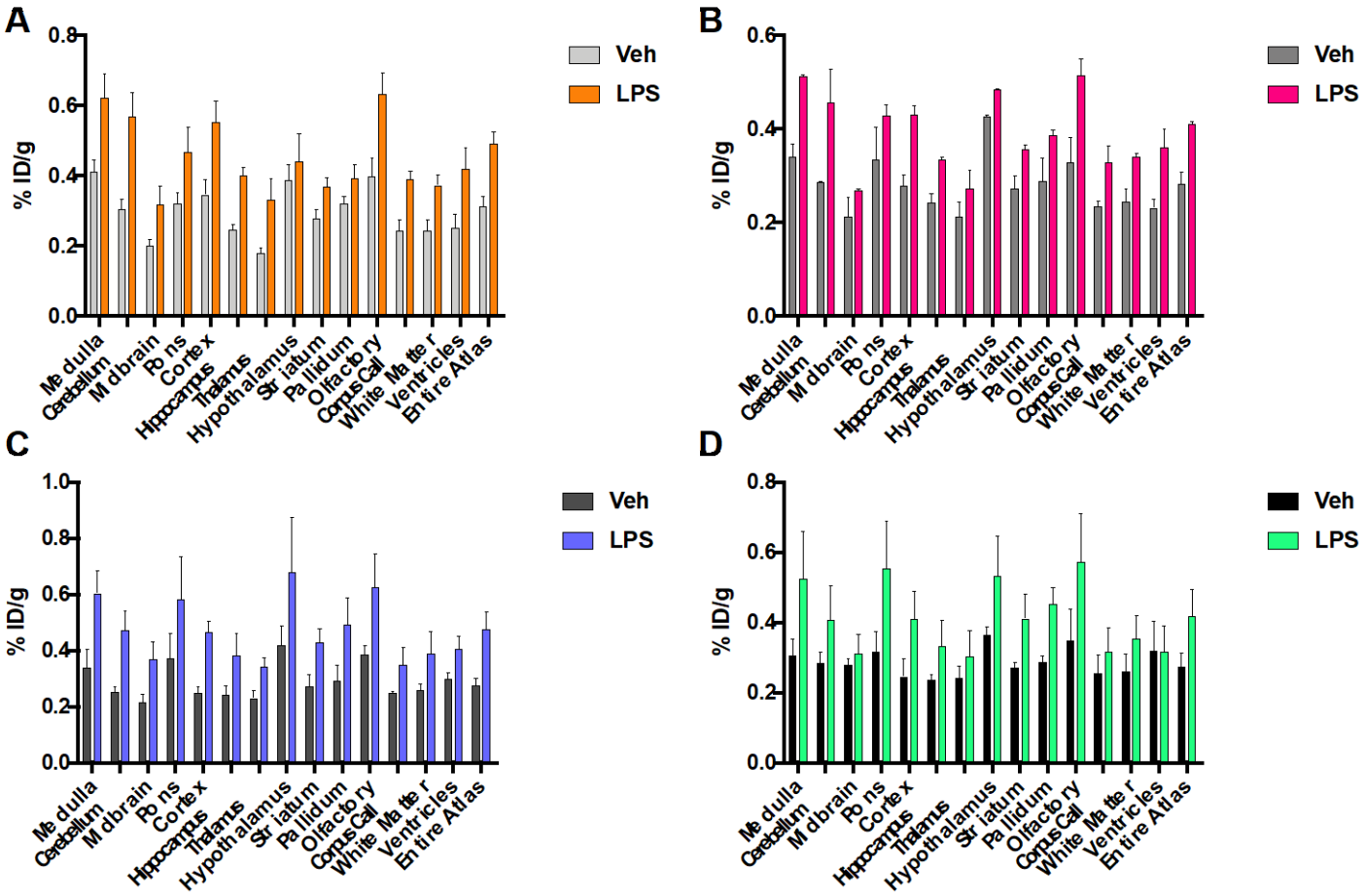

†**Supplemental Fig. 9**. Full brain PET quantitation of [^{64}Cu]Cu-NO2A-c[E_4W_5C] at 4 h (A), 8 h (B), 12 h (C), and 24 h (D) post-LPS injection corresponding with values tabulated in Supporting Table 4. Data is represented as average %ID/g ± SD with *n* = 4 animals/group.

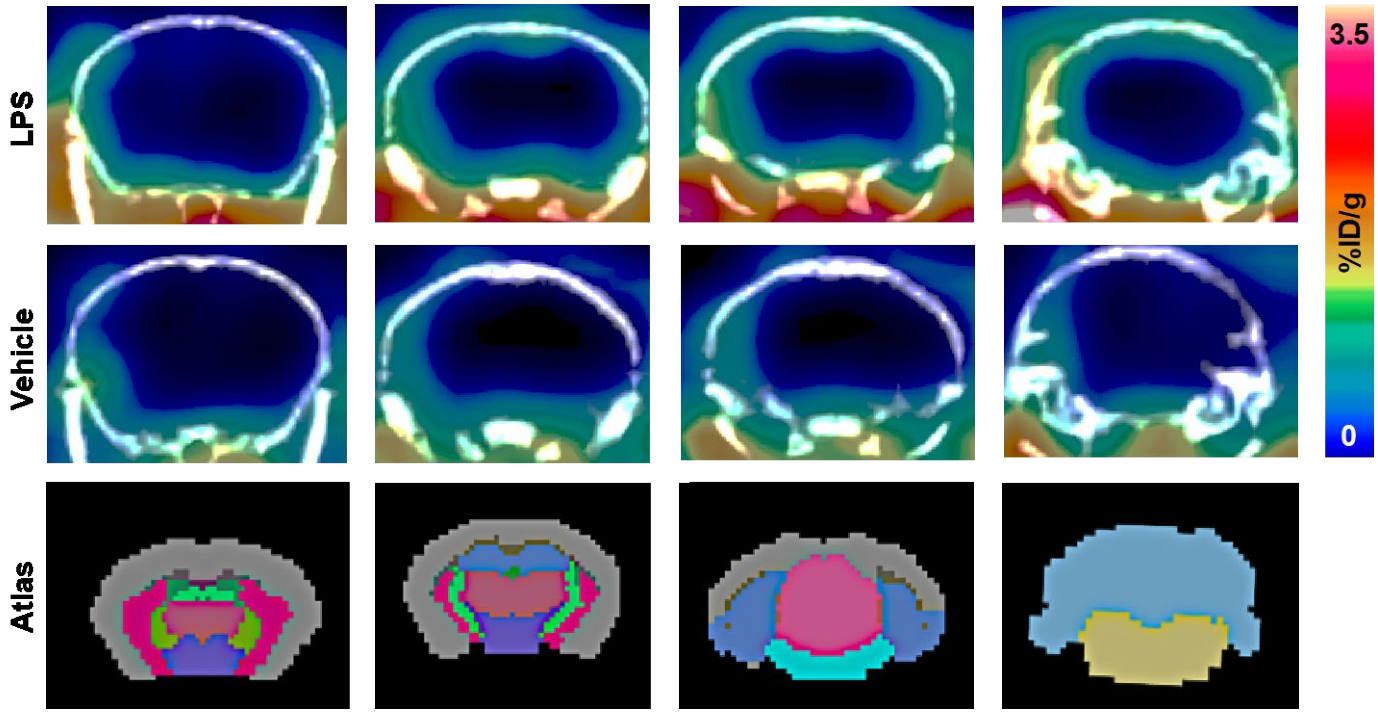

†**Supplemental Fig. 10**. Representative brain PET images of [^{64}Cu]Cu-NO2A-c[E$_4$W$_5$C] 4 h post-LPS injection (*n* = 4/group).

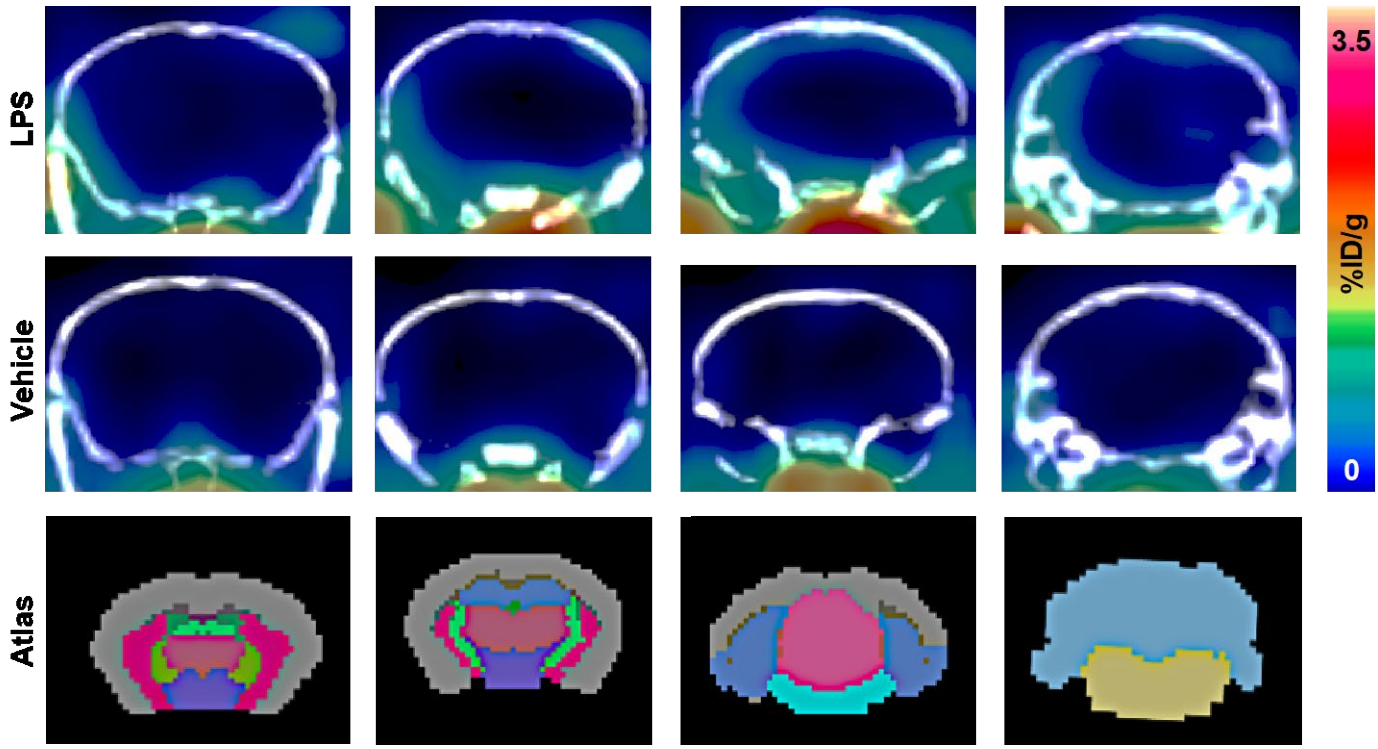

†**Supplemental Fig. 11**. Representative brain PET images of [^{64}Cu]Cu-NO2A-c[E$_4$W$_5$C] 8 h post-LPS injection (*n* = 4/group).

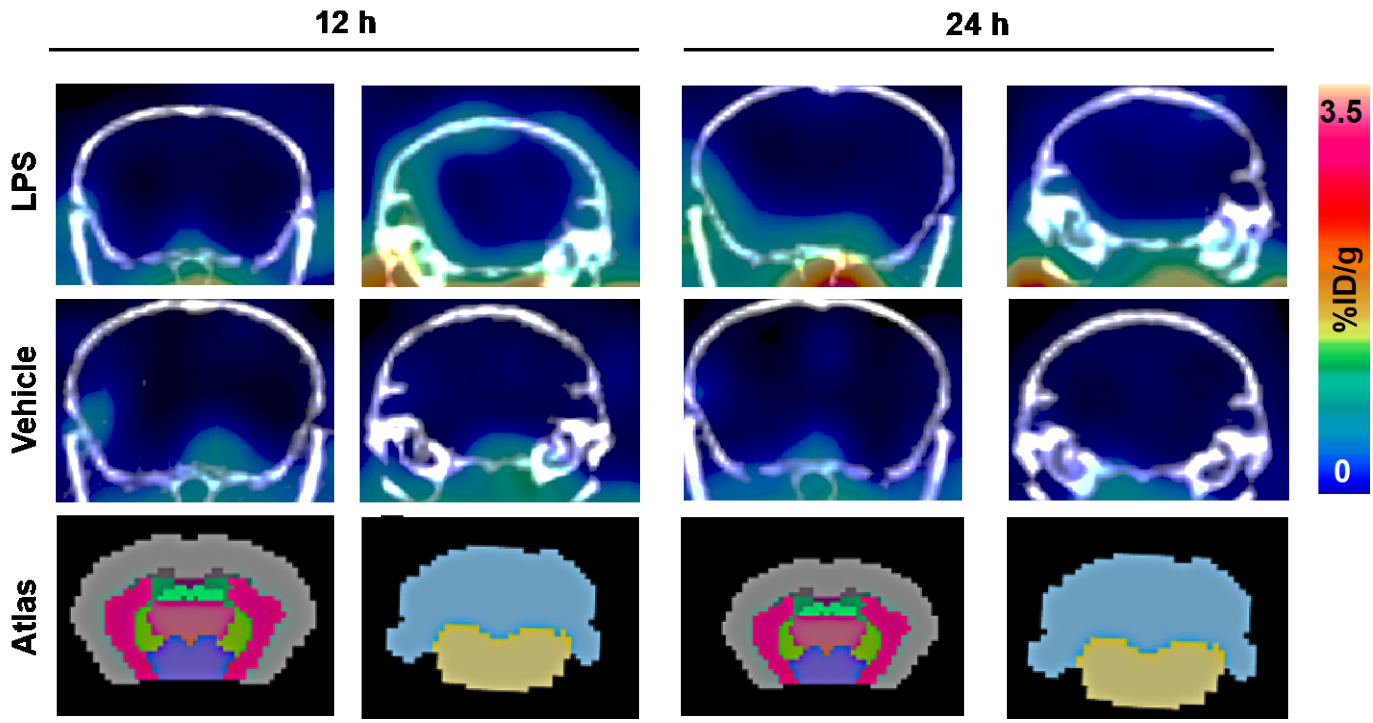

†**Supplemental Fig. 12**. Representative brain PET images of [^{64}Cu]Cu-NO2A-c[E$_4$W$_5$C] at 12 and 24 h-post injection with LPS. These views are showing the same representative mice shown in Fig. 4, but with additional views of the frontal cortex and cerebellum (*n* = 4/group).

Supplemental Fig. 13. Legend for inviCRO brain atlas represents segmentation algorithm used for PET quantitation.

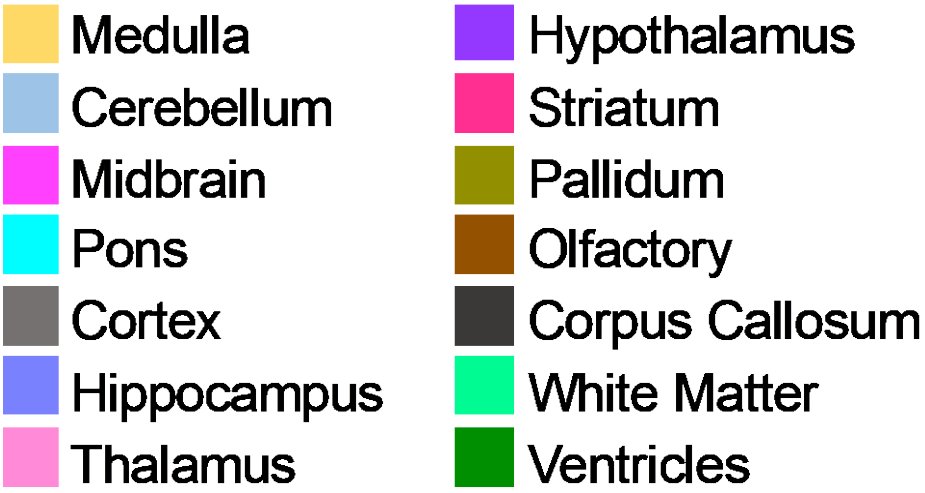

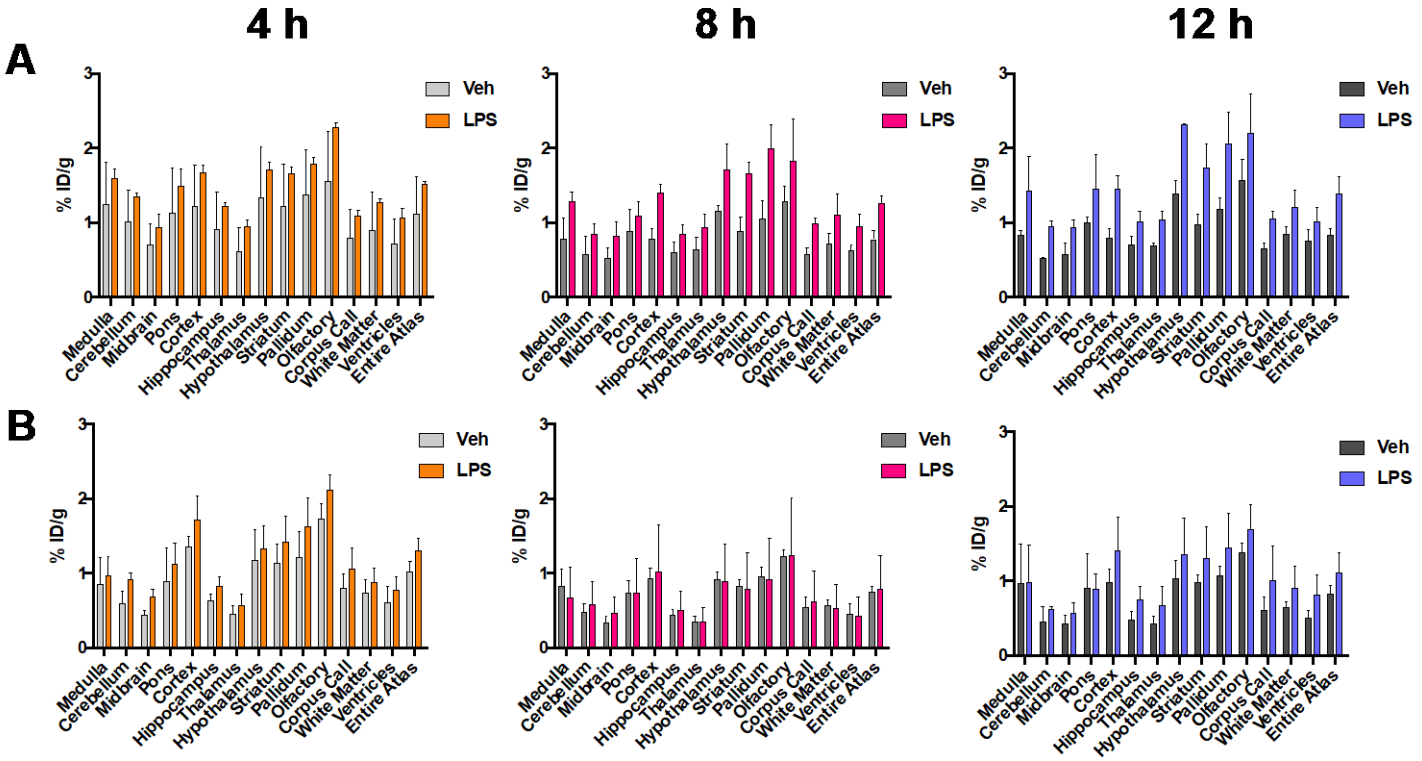

‡**Supplemental Fig. 14**. Full brain PET quantitation of and [^{64}Cu]Cu-NO2A-c[E_4W_5C] (A) and [^{64}Cu]Cu-NO2A-c[R_4W_5C] (B) at 4 h, 8 h, and 12 h post-LPS injection corresponding with values tabulated in Supporting Table 7. Data is represented as average %ID/g ± SD with *n* = 4 animals/group.

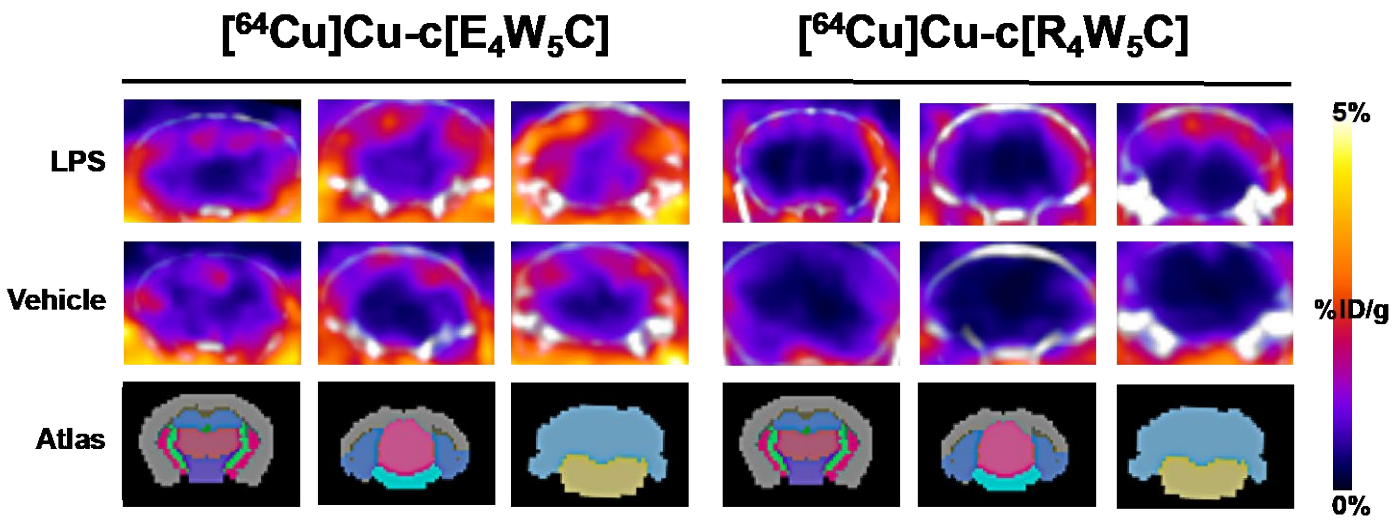

‡**Supplemental Fig. 15**. Representative brain PET images of [^{64}Cu]Cu-NO2A-c[E_4W_5C] vs. [^{64}Cu]Cu-NO2A-c[R_4W_5C] 4 h post-injection with LPS (selected from groups of *n* = 4).

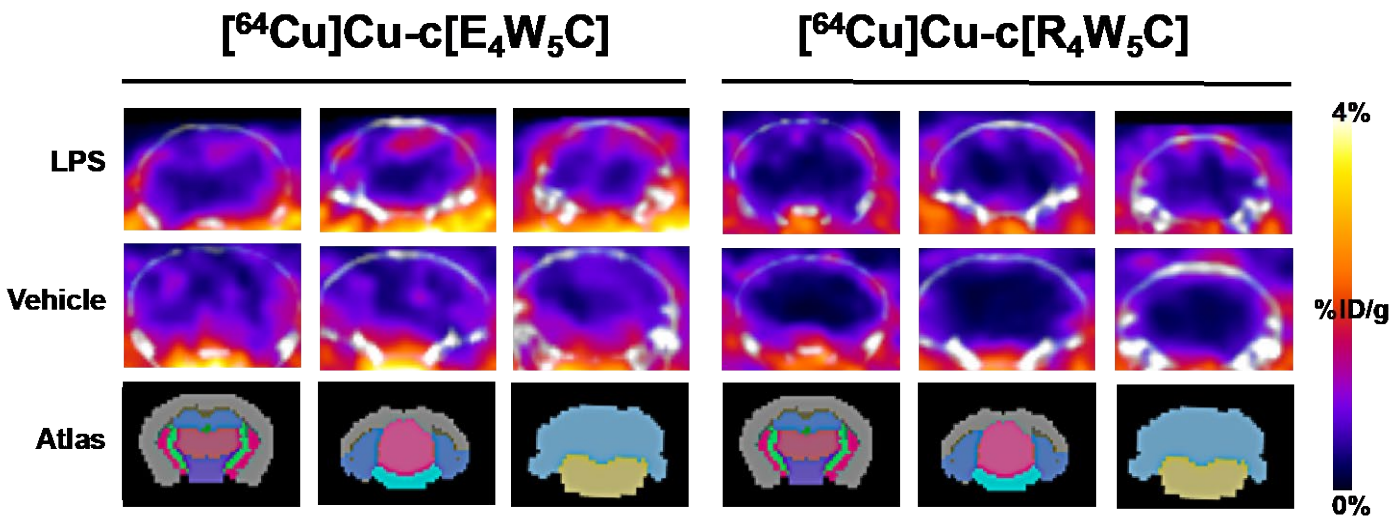

‡**Supplemental Fig. 16**. Representative brain PET images of [^{64}Cu]Cu-NO2A-c[E_4W_5C] vs. [^{64}Cu]Cu-NO2A-c[R_4W_5C] 8 h post-injection with LPS (selected from groups of *n* = 4).

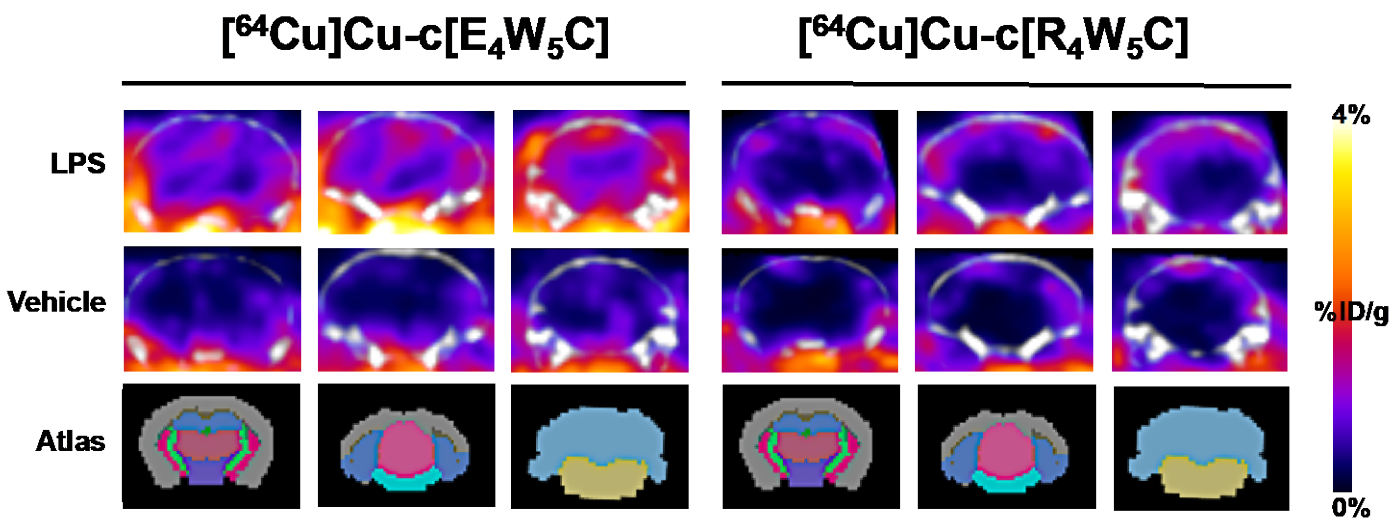

‡**Supplemental Fig. 17**. Representative brain PET images of [^{64}Cu]Cu-NO2A-c[E_4W_5C] vs. [^{64}Cu]Cu-NO2A-c[R_4W_5C] 12 h post-injection with LPS (selected from groups of *n* = 4).

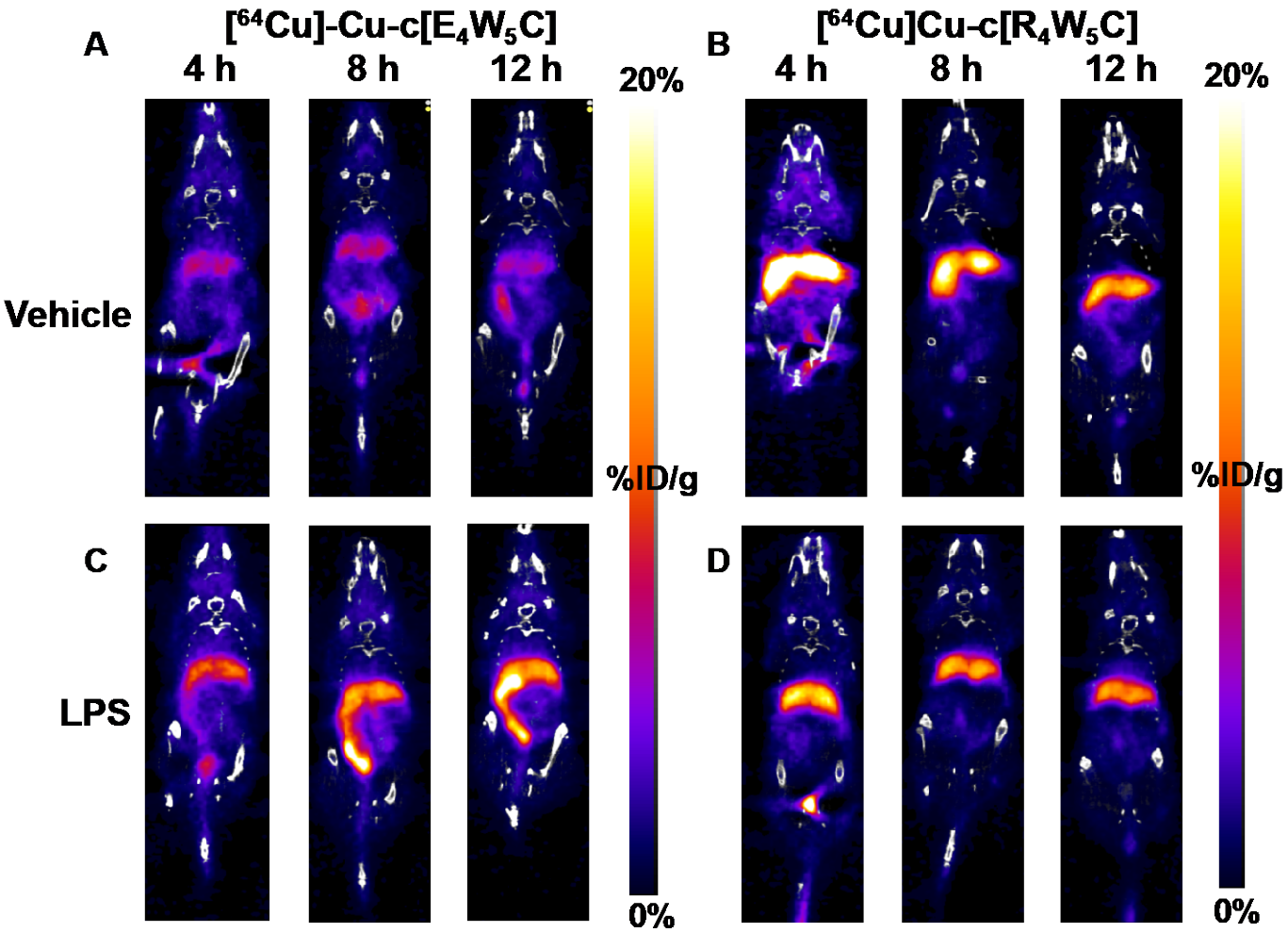
A
[64Cu]-Cu-c[E4W5C]
4 h
8 h
12 h
20%
B
[64Cu]Cu-c[R4W5C]
4 h
8 h
12 h
20%
Vehicle
%ID/g
%ID/g
C
D
LPS
0%
0%

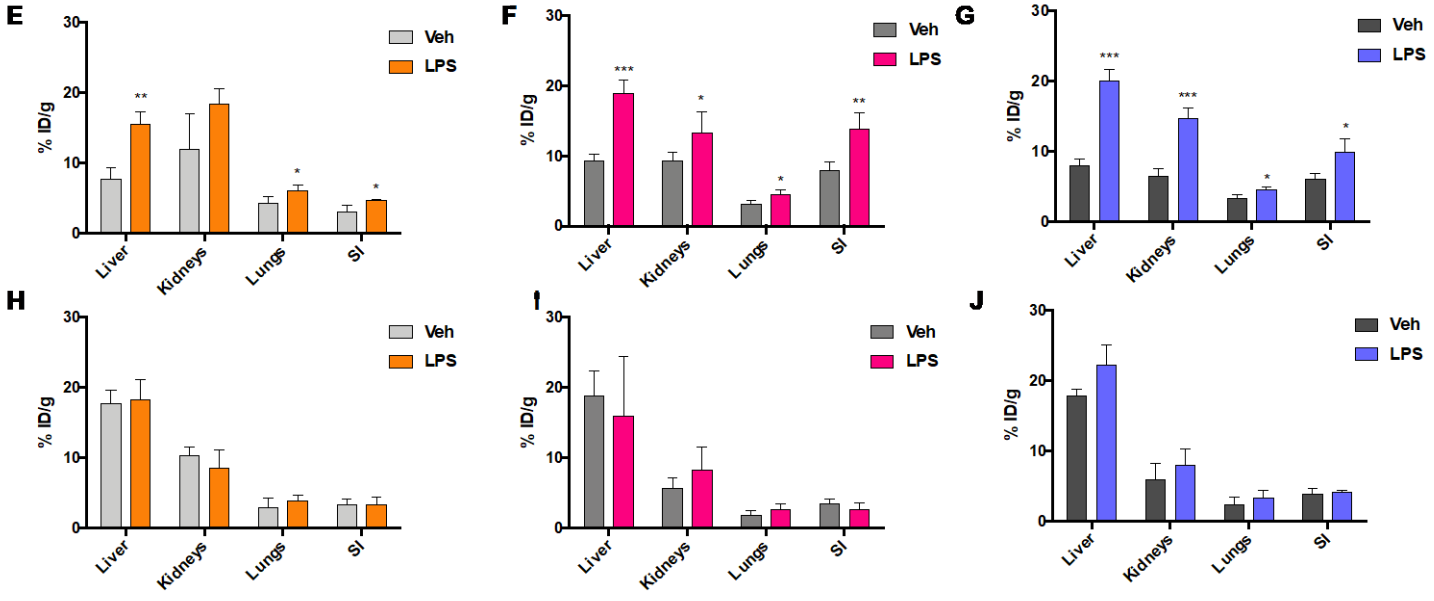
E
F
G
H
I
J
% ID/g
Veh
LPS
Liver
Kidneys
Lungs
SI

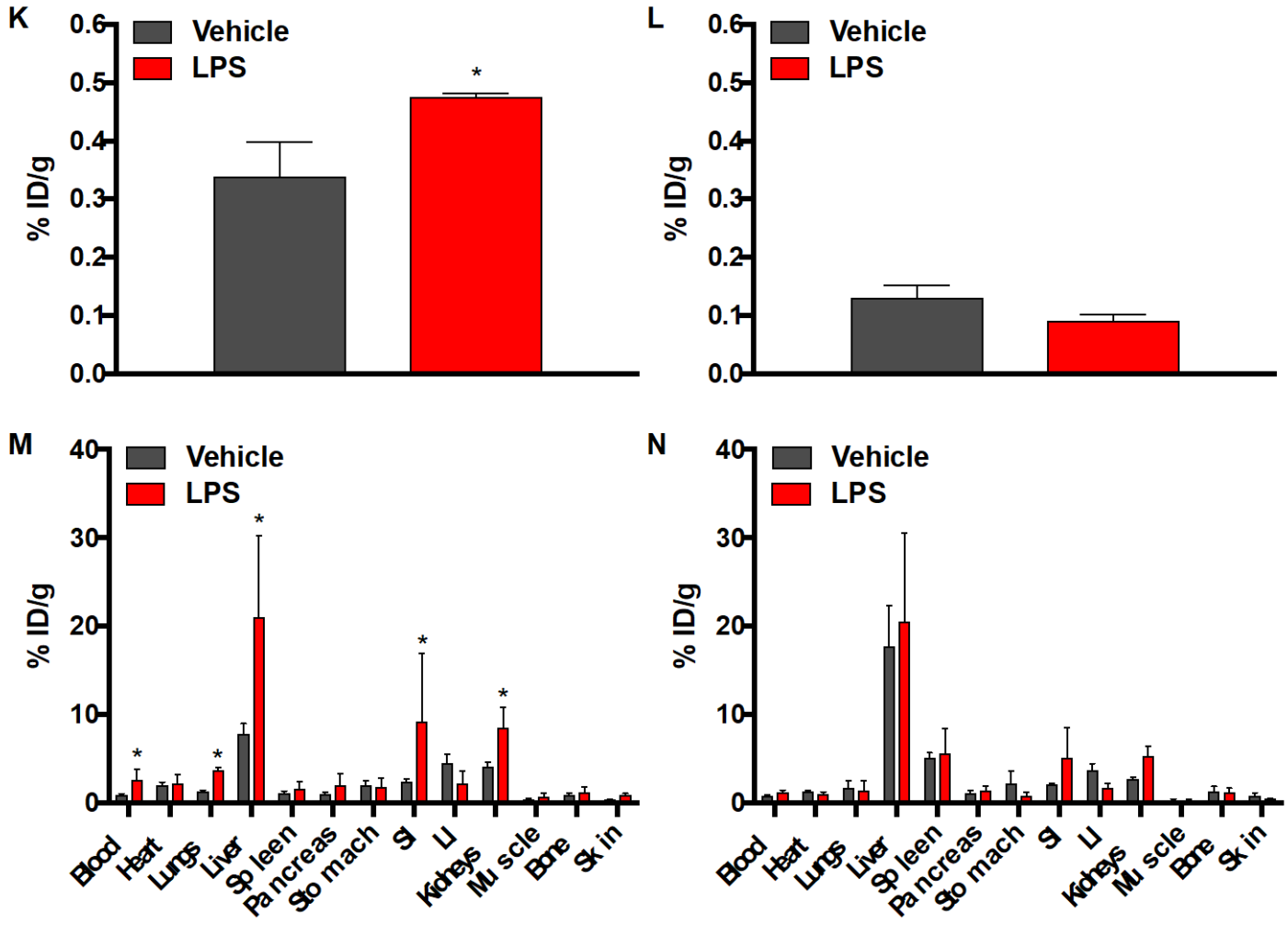

‡**Supplemental Fig. 18**. Serial PET imaging of [^{64}Cu]Cu-c[E_4W_5C] vs. [^{64}Cu]Cu-c[R_4W_5C] uptake in vehicle (A and B) vs. LPS-treated (C and D) mice over the course of 12 h (*n* = 4/group). Peripheral quantitation of PET organs was performed by manually drawing ROIs around select tissues at 4 h, 8 h, and 12 h post-LPS inoculation for [^{64}Cu]Cu-c[E_4W_5C] (E, F, and G, respectively) and [^{64}Cu]Cu-c[R_4W_5C] at 4 h, 8 h, and 12 h post-LPS (H, I, and J, respectively). Full biodistribution was performed at 24 h post-LPS injection (*n* = 4/group for vehicle, *n* = 2/LPS for group, per radiotracer). Brain uptake (K) and respective whole-body values (M) are shown for [^{64}Cu]Cu-c[E_4W_5C] pHLIC. Brain uptake (L) and respective values (N) are shown for [^{64}Cu]Cu-c[R_4W_5C] control. Tabulated values for peripheral PET and ex vivo biodistribution can be found in Supplemental Tables 8 and 9.

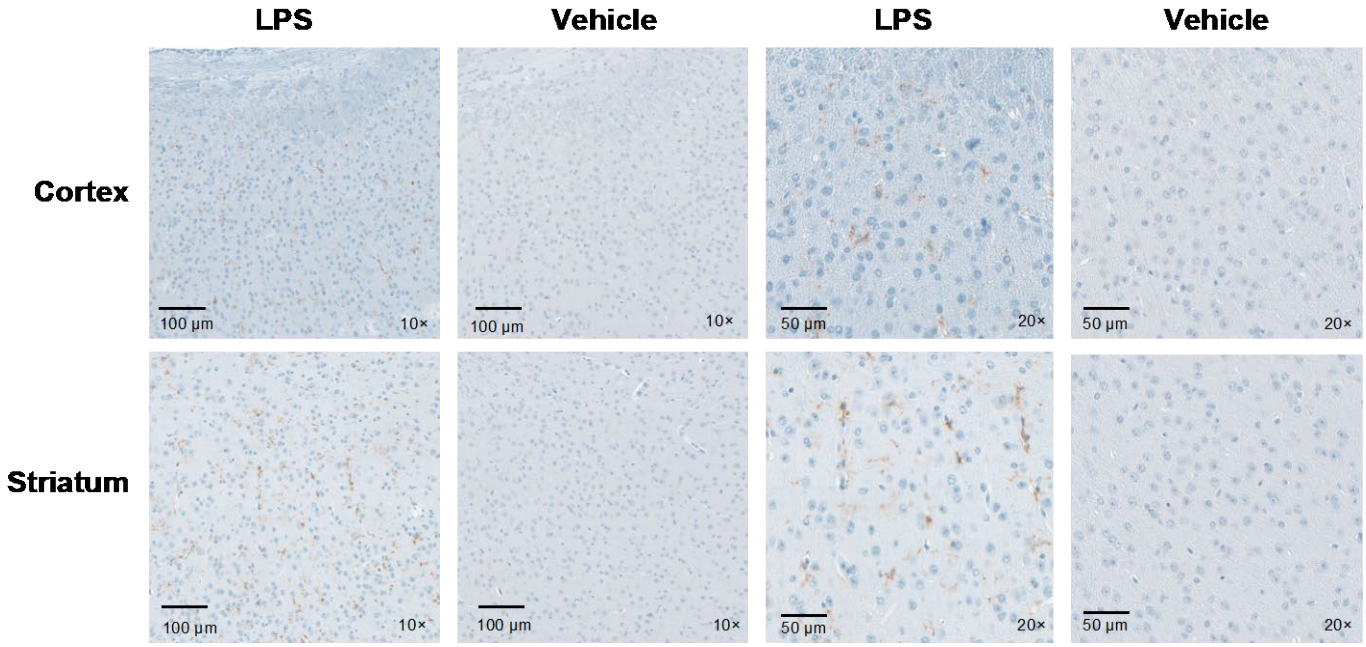

‡**Supplemental Fig. 19**. Immunohistochemical staining of TMEM119 show an increase in microglia in select brain regions of LPS-treated mice vs. vehicle (*n* = 3/group).

†**Supplemental Table 2**. Full ex vivo biodistribution of [^{64}Cu]Cu-[E$_5$K]W$_5$C at 24 h. Data is represented as average %ID/g ± SD with *n* = 4 animals/group. Abbreviations: SI: small intestine; LI: large intestine.

24 h			
Tissue	Vehicle	LPS	P value
Brain	0.14 ± 0.03	0.20 ± 0.06	0.134697
Blood	0.60 ± 0.11	2.23 ± 0.96	0.017429
Heart	1.13 ± 0.33	1.76 ± 0.93	0.256697
Lungs	2.00 ± 1.66	1.83 ± 1.29	0.893041
Liver	5.30 ± 1.87	26.06 ± 3.63	0.00017
Spleen	1.14 ± 0.63	1.77 ± 0.71	0.26613
Pancreas	0.61 ± 0.10	1.22 ± 0.69	0.114409
Stomach	0.54 ± 0.32	2.70 ± 1.86	0.065958
SI	1.98 ± 0.76	5.72 ± 5.32	0.19078
LI	5.20 ± 1.24	5.04 ± 4.48	0.946782
Kidneys	3.87 ± 1.55	5.92 ± 2.48	0.234547
Muscle	0.43 ± 0.14	0.93 ± 0.61	0.160568
Bone	0.66 ± 0.36	0.99 ± 0.46	0.332227
Skin	0.44 ± 0.21	1.03 ± 0.50	0.081138
Tail	0.36 ± 0.09	0.63 ± 0.29	0.13116

‡**Supplemental Table 3**. Full ex vivo biodistribution of [^{64}Cu]Cu-c[E_4W_5C] at 12 and 24 h (*n* = 4/group) with respective P values (as determined by unpaired two-tailed t-test) comparing vehicle and LPS-treated groups. Data is represented as average %ID/g ± SD with *n* = 4 animals/group.

12 h			
Tissue	Vehicle	LPS	P value
Brain	0.20 ± 0.05	0.25 ± 0.06	0.353235
Blood	1.08 ± 0.09	2.73 ± 1.43	0.117516
Heart	1.79 ± 0.42	2.71 ± 0.45	0.061524
Lungs	1.95 ± 0.62	2.82 ± 0.64	0.305098
Liver	10.24 ± 1.41	12.68 ± 3.71	0.34753
Spleen	2.60 ± 0.84	3.37 ± 0.30	0.205689
Pancreas	1.32 ± 0.41	2.29 ± 0.32	0.032566
Stomach	3.52 ± 1.66	3.20 ± 1.08	0.791259
SI	5.07 ± 1.04	11.71 ± 4.73	0.07658
LI	14.14 ± 2.94	4.60 ± 0.73	0.005475
Kidneys	7.13 ± 1.30	13.27 ± 2.54	0.020305
Muscle	0.31 ± 0.23	1.07 ± 0.15	0.008741
Bone	0.72 ± 0.16	1.34 ± 0.36	0.052285
Skin	1.35 ± 0.14	2.78 ± 1.46	0.164904

24 h			
Tissue	Vehicle	LPS	P value
Brain	0.29 ± 0.05	0.43 ± 0.04	0.000308
Blood	1.29 ± 0.27	3.60 ± 1.77	0.009368
Heart	2.35 ± 0.45	2.54 ± 0.45	0.469931
Lungs	1.94 ± 0.84	3.79 ± 1.49	0.032256
Liver	12.07 ± 1.56	23.84 ± 5.32	0.000793
Spleen	2.64 ± 0.92	3.80 ± 1.23	0.085074
Pancreas	1.24 ± 0.36	2.47 ± 0.85	0.007407
Stomach	1.59 ± 0.94	2.66 ± 1.81	0.222081
SI	4.36 ± 1.33	15.75 ± 6.78	0.002016
LI	10.04 ± 3.57	5.41 ± 4.18	0.057131
Kidneys	7.17 ± 1.98	9.74 ± 0.81	0.009285
Muscle	0.70 ± 0.26	1.19 ± 0.29	0.01123
Bone	1.23 ± 0.36	1.43 ± 0.53	0.468761
Skin	1.17 ± 0.27	2.47 ± 0.71	0.00139

†**Supplemental Table 4**. PET quantitation of [^{64}Cu]Cu-c[E_4W_5C] of select regions at 4, 8, 12, and 24 h post-LPS injection. Data is represented as average %ID/g ± SD with *n* = 4 animals/group. Abbreviations: SI: small intestine; LI: large intestine.

24 h			
Tissue	Vehicle	LPS	P value
Liver	5.99 ± 0.47	13.12 ± 2.91	7.34E-05
SI	5.26 ± 0.57	13.20 ± 3.68	0.000229
Kidneys	3.17 ± 0.62	6.59 ± 1.70	0.000562
Lungs	1.25 ± 0.13	1.99 ± 0.36	0.000419

12 h			
Tissue	Vehicle	LPS	P value
Liver	6.56 ± 0.99	13.63 ± 1.81	0.000473
SI	5.86 ± 0.65	12.07 ± 1.68	0.00046
Kidneys	5.90 ± 2.61	10.80 ± 2.49	0.035003
Lungs	1.18 ± 0.02	2.24 ± 0.38	0.001443

8 h			
Tissue	Vehicle	LPS	P value
Liver	9.00 ± 0.26	15.64 ± 0.58	8.14E-07
SI	8.66 ± 0.13	16.70 ± 1.15	8.81E-06
Kidneys	6.34 ± 0.74	11.03 ± 0.29	2.22E-05
Lungs	1.22 ± 0.06	2.06 ± 0.11	1.43E-05

4 h			
Tissue	Vehicle	LPS	P value
Liver	8.99 ± 2.37	18.49 ± 4.77	0.011877
SI	8.08 ± 2.23	16.83 ± 5.04	0.019203
Kidneys	8.46 ± 2.22	14.08 ± 3.62	0.058369
Lungs	1.73 ± 0.44	3.35 ± 0.88	0.01618

†**Supplemental Table 5**. Full PET quantitation of brain regions at 4, 8, 12, and 24 h post-LPS injection for [^{64}Cu]Cu-c[E_4W_5C]. Data is represented as average %ID/g ± SD with *n* = 4 animals/group. Abbreviations: Corpus Call: Corpus Callosum.

24 h			
Tissue	Vehicle	LPS	P value
Medulla	0.41 ± 0.12	0.76 ± 0.06	0.0018
Cerebellum	0.36 ± 0.07	0.56 ± 0.09	0.0265
Midbrain	0.30 ± 0.03	0.48 ± 0.09	0.0113
Pons	0.37 ± 0.08	0.75 ± 0.10	<0.0001
Cortex	0.28 ± 0.04	0.53 ± 0.08	0.0025
Hippocampus	0.29 ± 0.05	0.48 ± 0.10	0.0452
Thalamus	0.31 ± 0.07	0.42 ± 0.08	0.97
Hypothalamus	0.42 ± 0.07	0.90 ± 0.18	<0.0001
Striatum	0.34 ± 0.07	0.53 ± 0.07	0.0914
Pallidum	0.35 ± 0.06	0.62 ± 0.10	0.001
Olfactory	0.37 ± 0.05	0.62 ± 0.11	0.0098
Corpus Call	0.32 ± 0.06	0.45 ± 0.07	0.5863
White Matter	0.31 ± 0.05	0.49 ± 0.07	0.1875
Ventricles	0.39 ± 0.09	0.48 ± 0.06	0.9834
Entire Atlas	0.33 ± 0.05	0.56 ± 0.08	0.0067

12 h			
Tissue	Vehicle	LPS	P value
Medulla	0.34 ± 0.0643	0.60 ± 0.0805	<0.0001
Cerebellum	0.25 ± 0.0155	0.47 ± 0.0681	0.0005
Midbrain	0.22 ± 0.0290	0.37 ± 0.0601	0.0418
Pons	0.37 ± 0.0880	0.58 ± 0.1498	0.0011
Cortex	0.25 ± 0.0206	0.47 ± 0.0373	0.0006
Hippocampus	0.24 ± 0.0297	0.38 ± 0.0758	0.097
Thalamus	0.23 ± 0.0252	0.34 ± 0.0323	0.3633
Hypothalamus	0.42 ± 0.0706	0.68 ± 0.1957	<0.0001
Striatum	0.27 ± 0.0400	0.43 ± 0.0463	0.0318
Pallidum	0.29 ± 0.0551	0.49 ± 0.0934	0.0019
Olfactory	0.39 ± 0.0337	0.63 ± 0.1201	0.0001
Corpus Call	0.25 ± 0.0046	0.35 ± 0.0605	0.5486
White Matter	0.26 ± 0.0219	0.39 ± 0.0775	0.1633
Ventricles	0.30 ± 0.0194	0.41 ± 0.0456	0.4474
Entire Atlas	0.28 ± 0.0232	0.48 ± 0.0615	0.0024

8 h			
Tissue	Vehicle	LPS	P value
Medulla	0.34 ± 0.0269	0.51 ± 0.0023	<0.0001
Cerebellum	0.29 ± 0.0002	0.46 ± 0.0716	<0.0001
Midbrain	0.21 ± 0.0422	0.27 ± 0.0034	0.7013
Pons	0.34 ± 0.0678	0.43 ± 0.0213	0.0612
Cortex	0.28 ± 0.0221	0.43 ± 0.0168	0.0003
Hippocampus	0.24 ± 0.0184	0.34 ± 0.0047	0.0736
Thalamus	0.21 ± 0.0317	0.27 ± 0.0395	0.5882
Hypothalamus	0.43 ± 0.0032	0.48 ± 0.0016	0.6548
Striatum	0.27 ± 0.0278	0.36 ± 0.0089	0.1404
Pallidum	0.29 ± 0.0472	0.39 ± 0.0114	0.0535
Olfactory	0.33 ± 0.0518	0.52 ± 0.0342	<0.0001
Corpus Call	0.24 ± 0.0105	0.33 ± 0.0331	0.0587
White Matter	0.25 ± 0.0255	0.34 ± 0.0060	0.056
Ventricles	0.23 ± 0.0182	0.36 ± 0.0390	0.0029
Entire Atlas	0.28 ± 0.0250	0.41 ± 0.0038	0.0034

4 h			
Tissue	Vehicle	LPS	P value
Medulla	0.41 ± 0.0323	0.62 ± 0.0681	<0.0001
Cerebellum	0.30 ± 0.0278	0.57 ± 0.0677	<0.0001
Midbrain	0.20 ± 0.0175	0.32 ± 0.0522	0.003
Pons	0.32 ± 0.0299	0.47 ± 0.0719	0.0001
Cortex	0.35 ± 0.0432	0.55 ± 0.0599	<0.0001
Hippocampus	0.25 ± 0.0152	0.40 ± 0.0204	<0.0001
Thalamus	0.18 ± 0.0119	0.33 ± 0.0563	<0.0001
Hypothalamus	0.39 ± 0.0425	0.44 ± 0.0794	0.7646
Striatum	0.28 ± 0.0240	0.37 ± 0.0252	0.0611
Pallidum	0.32 ± 0.0192	0.39 ± 0.0388	0.3031
Olfactory	0.40 ± 0.0532	0.63 ± 0.0606	<0.0001
Corpus Call	0.24 ± 0.0315	0.39 ± 0.0224	<0.0001
White Matter	0.24 ± 0.0299	0.37 ± 0.0273	0.0009
Ventricles	0.25 ± 0.0370	0.42 ± 0.0576	<0.0001
Entire Atlas	0.31 ± 0.0259	0.49 ± 0.0327	<0.0001

‡**Supplemental Table 6**. A. Full PET quantitation of brain regions for [^{64}Cu]Cu-c[R$_4$W$_5$C] and [^{64}Cu]Cu-c[E$_4$W$_5$C] at 4, 8, and 12 h post-LPS injection. Data is represented as average %ID/g ± SD with *n* = 4 animals/group. Abbreviations: Corpus Call: Corpus Callosum. B. P values comparing LPS groups of [^{64}Cu]Cu-c[E$_4$W$_5$C] vs. LPS of [^{64}Cu]Cu-c[R$_4$W$_5$C].

A.

[^{64}Cu]Cu-c[E$_4$W$_5$]C 4 h			
Tissue	Vehicle	LPS	P value
Medulla	1.25 ± 0.5609	1.60 ± 0.1148	0.9867
Cerebellum	1.03 ± 0.4117	1.36 ± 0.0425	0.9925
Midbrain	0.71 ± 0.2843	0.94 ± 0.1681	0.9998
Pons	1.14 ± 0.5968	1.50 ± 0.2231	0.9851
Cortex	1.22 ± 0.5491	1.68 ± 0.0997	0.8847
Hippocampus	0.92 ± 0.5016	1.23 ± 0.0449	0.9953
Thalamus	0.63 ± 0.3106	0.96 ± 0.0875	0.9924
Hypothalamus	1.34 ± 0.6794	1.72 ± 0.0969	0.9755
Striatum	1.23 ± 0.5616	1.66 ± 0.0861	0.9208
Pallidum	1.38 ± 0.6004	1.80 ± 0.0854	0.9343
Olfactory	1.57 ± 0.6618	2.28 ± 0.0574	0.2632
Corpus Call	0.80 ± 0.3868	1.10 ± 0.0671	0.9968
White Matter	0.91 ± 0.4999	1.28 ± 0.0414	0.9731
Ventricles	0.73 ± 0.3198	1.07 ± 0.1294	0.9888
Entire Atlas	1.12 ± 0.4961	1.53 ± 0.0317	0.9544

[^{64}Cu]Cu-c[E$_4$W$_5$]C 8 h			
Tissue	Vehicle	LPS	P value
Medulla	0.78 ± 0.2847	1.29 ± 0.1236	0.068
Cerebellum	0.58 ± 0.2410	0.85 ± 0.1402	0.8532
Midbrain	0.53 ± 0.1328	0.83 ± 0.1918	0.875
Pons	0.89 ± 0.2858	1.09 ± 0.1944	0.9836
Cortex	0.78 ± 0.1364	1.41 ± 0.1048	0.0089
Hippocampus	0.61 ± 0.1341	0.85 ± 0.1243	0.9281
Thalamus	0.64 ± 0.1653	0.95 ± 0.1669	0.8495
Hypothalamus	1.17 ± 0.0641	1.71 ± 0.3452	0.0391
Striatum	0.89 ± 0.1870	1.66 ± 0.1595	0.0006
Pallidum	1.06 ± 0.2457	2.00 ± 0.3164	<0.0001
Olfactory	1.29 ± 0.1933	1.83 ± 0.5715	0.0447
Corpus Call	0.58 ± 0.0858	1.00 ± 0.0674	0.247
White Matter	0.73 ± 0.1295	1.11 ± 0.2685	0.3607
Ventricles	0.63 ± 0.0685	0.95 ± 0.1632	0.6392
Entire Atlas	0.78 ± 0.1146	1.26 ± 0.1011	0.0979

[^{64}Cu]Cu-c[E$_4$W$_5$]C 12 h			
Tissue	Vehicle	LPS	P value
Medulla	0.84 ± 0.0594	1.43 ± 0.4628	0.0263
Cerebellum	0.52 ± 0.0160	0.95 ± 0.0731	0.2657
Midbrain	0.59 ± 0.1377	0.95 ± 0.0930	0.5367
Pons	1.01 ± 0.0694	1.46 ± 0.4543	0.1885
Cortex	0.80 ± 0.1218	1.46 ± 0.1726	0.0083
Hippocampus	0.70 ± 0.1167	1.02 ± 0.1344	0.7389
Thalamus	0.70 ± 0.0376	1.04 ± 0.1078	0.7556
Hypothalamus	1.40 ± 0.1751	2.32 ± 0.0164	0.0004
Striatum	0.98 ± 0.1259	1.74 ± 0.3162	0.0013
Pallidum	1.19 ± 0.1403	2.07 ± 0.4068	0.0001
Olfactory	1.57 ± 0.2795	2.21 ± 0.5166	0.0125
Corpus Call	0.66 ± 0.0616	1.06 ± 0.1007	0.3912
White Matter	0.85 ± 0.0942	1.21 ± 0.2344	0.5445
Ventricles	0.76 ± 0.1489	1.02 ± 0.1888	0.9193
Entire Atlas	0.84 ± 0.0854	1.40 ± 0.2250	0.0478

[^{64}Cu]Cu-c[R$_4$W$_5$]C 4 h			
Tissue	Vehicle	LPS	P value
Medulla	0.85 ± 0.3509	0.98 ± 0.2381	>0.9999
Cerebellum	0.61 ± 0.1526	0.93 ± 0.0764	0.6146
Midbrain	0.44 ± 0.0613	0.69 ± 0.0936	0.9003
Pons	0.90 ± 0.4364	1.13 ± 0.2762	0.9572
Cortex	1.36 ± 0.1422	1.72 ± 0.3262	0.4365
Hippocampus	0.64 ± 0.0860	0.84 ± 0.1126	0.9885
Thalamus	0.46 ± 0.1028	0.57 ± 0.1568	>0.9999
Hypothalamus	1.18 ± 0.4057	1.34 ± 0.2991	0.9987
Striatum	1.15 ± 0.2427	1.42 ± 0.3495	0.8262
Pallidum	1.22 ± 0.3362	1.63 ± 0.3765	0.2459
Olfactory	1.73 ± 0.2030	2.13 ± 0.2000	0.274
Corpus Call	0.80 ± 0.1871	1.06 ± 0.2804	0.8945
White Matter	0.74 ± 0.1713	0.88 ± 0.1912	0.9997
Ventricles	0.62 ± 0.1991	0.78 ± 0.1760	0.9985
Entire Atlas	1.02 ± 0.1380	1.31 ± 0.1586	0.7897

[^{64}Cu]Cu-c[R$_4$W$_5$]C 8 h			
Tissue	Vehicle	LPS	P value
Medulla	0.84 ± 0.2166	0.68 ± 0.4077	>0.9999
Cerebellum	0.48 ± 0.1086	0.58 ± 0.3103	>0.9999
Midbrain	0.34 ± 0.0807	0.47 ± 0.2217	>0.9999
Pons	0.74 ± 0.1597	0.74 ± 0.4566	>0.9999
Cortex	0.93 ± 0.1353	1.02 ± 0.6332	>0.9999
Hippocampus	0.44 ± 0.0803	0.51 ± 0.2429	>0.9999
Thalamus	0.36 ± 0.0631	0.36 ± 0.1825	>0.9999
Hypothalamus	0.92 ± 0.0953	0.90 ± 0.4926	>0.9999
Striatum	0.84 ± 0.0735	0.79 ± 0.4829	>0.9999
Pallidum	0.97 ± 0.1147	0.92 ± 0.5532	>0.9999
Olfactory	1.24 ± 0.0785	1.24 ± 0.7622	>0.9999
Corpus Call	0.55 ± 0.1355	0.62 ± 0.4047	>0.9999
White Matter	0.58 ± 0.0740	0.54 ± 0.3092	>0.9999
Ventricles	0.46 ± 0.1284	0.43 ± 0.2564	>0.9999
Entire Atlas	0.75 ± 0.0673	0.79 ± 0.4478	>0.9999

[^{64}Cu]Cu-c[R$_4$W$_5$]C 12 h			
Tissue	Vehicle	LPS	P value
Medulla	0.97 ± 0.5238	0.99 ± 0.4925	>0.9999
Cerebellum	0.46 ± 0.1955	0.63 ± 0.0371	0.9998
Midbrain	0.43 ± 0.1039	0.57 ± 0.1393	>0.9999
Pons	0.91 ± 0.4497	0.90 ± 0.1958	>0.9999
Cortex	0.99 ± 0.1672	1.41 ± 0.4427	0.5378
Hippocampus	0.49 ± 0.1035	0.75 ± 0.1821	0.9762
Thalamus	0.44 ± 0.0829	0.67 ± 0.2511	0.9917
Hypothalamus	1.04 ± 0.2369	1.36 ± 0.4835	0.88
Striatum	0.99 ± 0.0891	1.31 ± 0.4217	0.8977
Pallidum	1.08 ± 0.1151	1.45 ± 0.4605	0.7245
Olfactory	1.38 ± 0.1291	1.70 ± 0.3253	0.8813
Corpus Call	0.61 ± 0.1808	1.01 ± 0.4529	0.6014
White Matter	0.66 ± 0.0717	0.92 ± 0.2861	0.9766
Ventricles	0.51 ± 0.1010	0.82 ± 0.2696	0.9111
Entire Atlas	0.83 ± 0.1128	1.11 ± 0.2655	0.9552

B.

Region	4 h	8 h	12 h
Medulla	0.0231	0.0237	0.3240
Cerebellum	0.0003	0.1891	0.0023
Midbrain	0.1038	0.1752	0.0176
Pons	0.1739	0.1498	0.1193
Cortex	0.2731	0.4181	0.8739
Hippocampus	0.0081	0.1195	0.1087
Thalamus	0.0329	0.0484	0.1546
Hypothalamus	0.1370	0.0530	0.0776
Striatum	0.5405	0.0577	0.2232
Pallidum	0.7454	0.0537	0.1572
Olfactory	0.3284	0.3285	0.2250
Corpus Call	0.5453	0.3013	0.8729
White Matter	0.0457	0.0680	0.2441
Ventricles	0.1240	0.0616	0.3451
Entire Atlas	0.1217	0.1720	0.2305

‡**Supplemental Table 7**. A. PET quantitation of [^{64}Cu]Cu-c[R$_4$W$_5$C] and [^{64}Cu]Cu-c[E$_4$W$_5$C] of select peripheral regions at 4, 8, and 12 h post-LPS injection. Data is represented as average %ID/g ± SD with *n* = 4 animals/group. P values comparing LPS groups of [^{64}Cu]Cu-c[E$_4$W$_5$C] vs. LPS of [^{64}Cu]Cu-c[R$_4$W$_5$C].

A.

[^{64}Cu]Cu-c[E$_4$W$_5$C]

12 h			
Tissue	Vehicle	LPS	P value
Liver	8.09 ± 0.86	20.10 ± 1.54	4.28E-05
SI	6.15 ± 0.73	10.01 ± 1.80	0.01071
Kidneys	6.50 ± 1.03	14.72 ± 1.45	0.000306
Lungs	3.35 ± 0.53	4.60 ± 0.41	0.020156

8 h			
Tissue	Vehicle	LPS	P value
Liver	9.38 ± 0.86	18.97 ± 1.78	0.000207
SI	8.02 ± 1.13	13.80 ± 2.38	0.007492
Kidneys	9.35 ± 1.19	13.33 ± 2.94	0.053726
Lungs	3.12 ± 0.50	4.50 ± 0.64	0.023478

4 h			
Tissue	Vehicle	LPS	P value
Liver	7.80 ± 1.59	15.55 ± 1.79	0.001754
SI	3.06 ± 0.96	4.77 ± 0.09	0.036791
Kidneys	11.96 ± 5.01	18.52 ± 2.14	0.090854
Lungs	4.42 ± 0.84	6.18 ± 0.68	0.032067

[^{64}Cu]Cu-c[R$_4$W$_5$C]

12 h			
Tissue	Vehicle	LPS	P value
Liver	17.85 ± 0.86	22.24 ± 2.81	0.060934
SI	3.81 ± 0.79	4.21 ± 0.14	0.433827
Kidneys	5.96 ± 2.24	8.01 ± 2.24	0.285222
Lungs	2.30 ± 1.11	3.28 ± 1.09	0.297125

8 h			
Tissue	Vehicle	LPS	P value
Liver	18.94 ± 3.42	16.04 ± 8.48	0.549311
SI	3.48 ± 0.68	2.76 ± 0.82	0.225002
Kidneys	5.78 ± 1.37	8.34 ± 3.25	0.197844
Lungs	1.96 ± 0.59	2.78 ± 0.70	0.122158

4 h			
Tissue	Vehicle	LPS	P value
Liver	17.85 ± 1.80	18.42 ± 2.79	0.745327
SI	3.43 ± 0.78	3.38 ± 1.01	0.936461
Kidneys	10.44 ± 1.17	8.55 ± 2.60	0.234361
Lungs	3.04 ± 1.24	3.96 ± 0.73	0.247581

B.

12 h	
Tissue	P value
Liver	0.311215
SI	0.01219
Kidneys	0.120675
Lungs	0.005155

8 h	
Tissue	P value
Liver	0.589591
SI	0.091147
Kidneys	0.020825
Lungs	0.000309

4 h	
Tissue	P value
Liver	0.333823
SI	0.009154
Kidneys	0.027715
Lungs	0.144527

‡**Supplemental Table 8**. A. Full ex vivo biodistribution of [^{64}Cu]Cu-c[R_4W_5C] and [^{64}Cu]Cu-c[E_4W_5C] with respective P values (as determined by unpaired two-tailed t-test) comparing vehicle and LPS-treated groups at 24 h-post LPS administration. Data is represented as average %ID/g ± SD (*n* = 4/group for vehicle, *n* = 2/LPS for group). P values comparing LPS groups of [^{64}Cu]Cu-c[E_4W_5C] vs. LPS of [^{64}Cu]Cu-c[R_4W_5C].

A.

[^{64}Cu]Cu-c[E_4W_5C]				[^{64}Cu]Cu-c[R_4W_5C]			
Tissue	Vehicle	LPS	P value	Tissue	Vehicle	LPS	P value
Blood	0.98 ± 0.18	2.58 ± 1.28	0.0231	Blood	0.94 ± 0.08	1.18 ± 0.31	0.2357
Heart	2.01 ± 0.35	2.23 ± 0.97	0.6473	Heart	1.21 ± 0.10	0.99 ± 0.32	0.2778
Lungs	1.76 ± 0.93	3.70 ± 0.30	0.0402	Lungs	1.63 ± 0.80	1.45 ± 1.30	0.8131
Liver	8.22 ± 1.27	20.98 ± 9.22	0.0161	Liver	18.54 ± 4.58	20.57 ± 12.23	0.7457
Spleen	1.17 ± 0.27	1.58 ± 0.85	0.3258	Spleen	5.25 ± 0.57	5.59 ± 3.51	0.8305
Pancreas	1.00 ± 0.25	1.99 ± 1.30	0.1157	Pancreas	1.18 ± 0.28	1.41 ± 0.66	0.5319
Stomach	2.10 ± 0.55	1.77 ± 1.00	0.5761	Stomach	1.82 ± 1.37	0.82 ± 0.53	0.3487
SI	2.64 ± 0.56	10.74 ± 5.54	0.0123	SI	2.97 ± 0.14	5.16 ± 4.18	0.3340
LI	4.68 ± 0.95	2.20 ± 1.42	0.0379	LI	3.10 ± 0.77	1.69 ± 0.70	0.1630
Kidneys	4.53 ± 1.05	8.47 ± 2.32	0.0200	Kidneys	3.47 ± 0.20	5.36 ± 1.29	0.1333
Muscle	0.44 ± 0.13	0.70 ± 0.43	0.2243	Muscle	0.35 ± 0.08	0.34 ± 0.14	0.9149
Bone	0.90 ± 0.26	1.22 ± 0.57	0.3597	Bone	1.27 ± 0.60	1.27 ± 0.52	0.9857
Skin	0.42 ± 0.06	0.95 ± 0.12	0.0004	Skin	0.76 ± 0.28	0.52 ± 0.02	0.2911
Brain	0.34 ± 0.06	0.48 ± 0.01	0.0264	Brain	0.12 ± 0.02	0.09 ± 0.01	0.2129

B.

Tissue	P value
Blood	0.271416
Heart	0.229126
Lungs	0.138901
Liver	0.973091
Spleen	0.257107
Pancreas	0.631845
Stomach	0.358247
SI	0.373264
LI	0.693616
Kidneys	0.238848
Muscle	0.379655
Bone	0.939168
Skin	0.041169
Brain	0.000693

REFERENCES

1. Shen C, Menon R, Das D, Bansal N, Guduru N, Jaegle S, Reshetnyak Y. K. The protein fluorescence and structural toolkit: Database and programs for the analysis of protein fluorescence and structural data. Proteins. 2008;71(4):1744-54.
2. Dierckx RA, de Wiele CV. FDG uptake, a surrogate of tumour hypoxia? Eur J Nuc Med and Mol Imag. 2008;35(8), 1544-1549.
3. Longo DL, Bartoli A, Consolino L, Bardini P, Arena F, Schwaiger M, Aime S. In Vivo Imaging of Tumor Metabolism and Acidosis by Combining PET and MRI-CEST pH Imaging. Cancer Res. 2016;76(22):6463-6470.
4. Hoiland, RL, Bain, AR, Rieger, MG, Bailey,2 DM, Ainslie, PN. Hypoxemia, oxygen content, and the regulation of cerebral blood flow. Am J Physiol Regul Comp Physiol. 2016;310(5): R398-R413.
5. Michael T. Alkire, MT, Pomfrett, CJD, Haier, RJ, Gianzero, MV, Chan, CM, Jacobsen, BP, Fallon JH. Functional Brain Imaging during Anesthesia in Humans: Effects of Halothane on Global and Regional Cerebral Glucose Metabolism. Clin Sci. 1999;90(3): 701-709.
6. Alstrup, AKO, Landau, AM, Holden, JE, Jakobsen S, Schacht, AC, Audrain, H, Wegener G, Hansen AK, Gjedde, A, Doudet, DJ. Effects of Anesthesia and Species on the Uptake or Binding of Radioligands In Vivo in the Göttingen Minipig. Biomed Res Int. 2013; 2013: 808713.